Supplementary Information (SI) for Journal of Materials Chemistry A.
This journal is © The Royal Society of Chemistry 2024

Supporting Information

From Structure to Electrochemistry: The Influence of Transition Metal Ordering on Na^+/vacancy Orderings in P2-type Na_xMO_2 Cathode Materials for Sodium-Ion Batteries

Lukas Fridolin Pfeiffer,[a] Manuel Dillenz,[b] Nora Burgard,[a] Premysl Beran,[c,d] Daniel Roscher,[e,f] Maider Zarrabeitia,[e,f] Paul Drews,[a] Charles Hervoches,[c] Daria Mikhailova,[g] Ahmad Omar,[g] Volodymyr Baran,[h] Neelima Paul,[i] Mohsen Sotoudeh,[b] Michael Busch,[j,k] Margret Wohlfahrt-Mehrens,[a] Axel Groß,[b] Stefano Passerini,[e,f] Peter Axmann*[a]*

[a] *ZSW Center for Solar Energy and Hydrogen Research Baden-Württemberg, Helmholtzstraße 8, 89081 Ulm, Germany.*

[b] *Institute for Theoretical Chemistry, Mez-Starck-Haus, Oberberghof 7, 89081 Ulm, Germany.*

[c] *Nuclear Physics Institute, CAS, Hlavni 130, 250 68 Rez, Czech Republic.*

[d] *European Spallation Source, ERIC, POBox 176, 221 00 Lund, Sweden.*

[e] *Helmholtz Institute Ulm, Helmholtzstraße 11, 89081 Ulm, Germany.*

[f] *Karlsruhe Institute of Technology, 76021 Karlsruhe, Germany.*

[g] *Leibniz Institute for Solid State and Materials Research (IFW) Dresden e.V., Helmholtzstr. 20, 01069 Dresden, Germany.*

[h] *Deutsches Elektronen-Synchrotron (DESY), Notkestraße 85, 22607 Hamburg, Germany.*

[i] *Heinz Maier-Leibnitz Zentrum, Technische Universität München, Lichtenbergstraße 1, 85747 Garching, Germany.*

[j] *Division of Materials Science, DepVartent of Engineering Sciences and Methematics, Luleå University of Technology, 971 87 Luleå, Sweden.*

[k] *Wallenberg Initiative Materials Science for Sustainability (WISE), Luleå University of Technology, 971 87 Luleå, Sweden.*

Supplementary Information: Entropymetry

Expectations - **Supplementary Figure S1** schematically depicts the influence of preferential site occupation on the course of the entropy S and entropy change ΔS. On the left side of **Supplementary Figure S1**, sodium ions are extracted from a two-dimensional unit cell consisting of four sodium ions neglecting any repulsion between these ions. The entropy S is calculated according to Boltzmann's formula

$$S = k_B \ln(\Omega) \tag{1}$$

where k_B is the Boltzmann constant and Ω is the number of possible arrangements. With four sodium ions on four sites ($Na_4\square_0$, where □ represents a vacancy), all lattice sites are occupied and solely one arrangement (blue) exists. Consequently, the entropy is calculated to be 0 J mol^{-1} K^{-1}. Removing one sodium ion ($Na_3\square_1$) leads to four possible configurations. Consequently, the entropy increases (cyan). If another sodium ion is removed ($Na_2\square_2$), two vacancies are present (green), which leads to six different unit cell arrangements causing a local maximum of the entropy. The extraction of one more ion ($Na_1\square_3$) is followed by a reduction of the entropy (orange, red). Hence, the course of the entropy represents a parabola. The entropy change ΔS can be derived by calculating the partial derivative of the entropy curve. If any Na-Na repulsion can be neglected (entropy curve equals a parabola), the entropy change follows a simple S-curve.

In reality, the repulsion between sodium ions cannot be neglected. Therefore, sodium ion configurations with maximized Na-Na distance will be favoured over configurations with sodium ions in close proximity to another. This scenario is depicted on the right side of **Supplementary Figure S1**. As a consequence, when two ions remain in the unit cell ($Na_2\square_2$, green), only diagonal lattice sites are occupied, transforming the local maximum of the parabola into a local minimum. Hence for preferential site occupancy the local entropy change follows a distinct double-s shape curve.

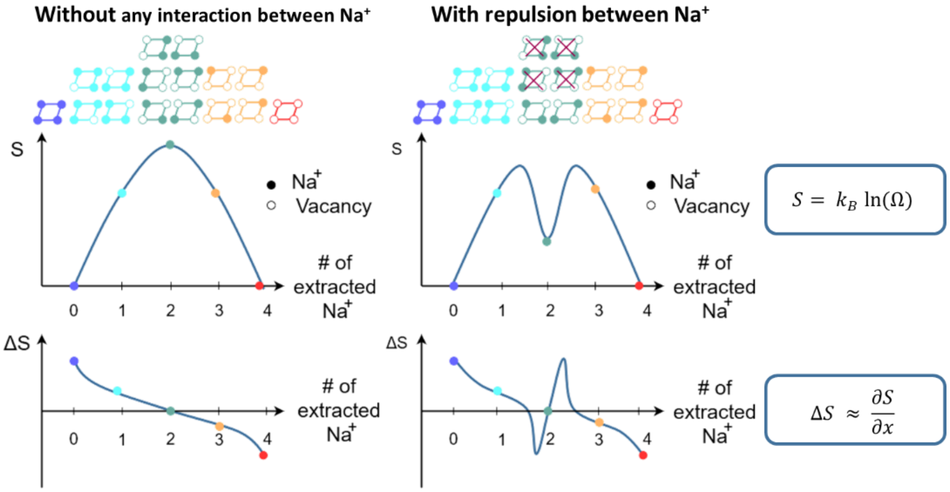

Supplementary Figure S1. *Schematic representation of configurational entropy change, (left) neglecting any Na-Na repulsion and (right) taking Na-Na repulsion into account.*

Thermodynamics - Making use of thermodynamic potentials, the cell potential E can be expressed through the Gibbs free energy ΔG as follows [1]:

$$E = \frac{-\Delta G}{n\,F} \tag{2}$$

Where n is the number of electrons and F is the Faraday constant. With the help of the term

$$\Delta G = \Delta H - T\,\Delta S \tag{3}$$

the expression can be rewritten as:

$$E = \frac{-\Delta H + T\,\Delta S}{n\,F} \tag{4}$$

Here, H is the enthalpy, T the temperature and S the entropy. Performing the partial derivative with regard to the temperature and rearranging leads to an applicable formula for the calculation of the entropy change. Since the potential is linearly dependent on the temperature for small changes, the partial derivative can be approximated as:

$$\Delta S = n\,F\,\frac{\Delta E}{\Delta T} \tag{5}$$

Therefore, the measurement of the relaxed cell potential during a temperature change delivers the data that is necessary to calculate the entropy change.

Experimental – Following the thermodynamic considerations, the entropy change of a system can be derived from the change of the potential with the temperature in a thermodynamically relevant state. For layered transition metal oxides (AMO_2, A = alkali metal, M = transition metals) at room temperature, the transitional metal oxide MO_2 can be considered as a stable and fixed host (for infinitesimal small changes of sodium content). Thermodynamically (meta)stable compositions A_xMO_2 can be screened by electrochemical titration of the alkali metal ion (*A*) within the host structure (*MO_2*) following the Galvanostatic Intermittant Titration Technique (GITT). After relaxation, the distribution of the alkali metal guest ions inside the stable host structure represents a thermodynamically relevant (meta-)stable state. Therefore, the measured potential can be used to describe the thermodynamic (meta)stable system and the entropy change can be derived from a GITT measurement including temperature change as described above.

In our labs, we have constructed coin-type half cells with a sodium metal counter electrode. These cells were connected to a potentiostat and placed in a programmable climate chamber. A representative extract of the GITT procedure with temperature change and the corresponding measured potential is presented in **Supplementary Figure S2**. At 40°C, current pulses were applied for 10 min. Subsequently, the cell was enabled to relax at open circuit voltage (OCV) for 8h, followed by a change in temperature to 25°C and 10°C for 2h each. During the 12h of OCV time, the cell voltage was observed. The entropy change was calculated from the linear regression of the cell voltage with the temperature according to equation (5).

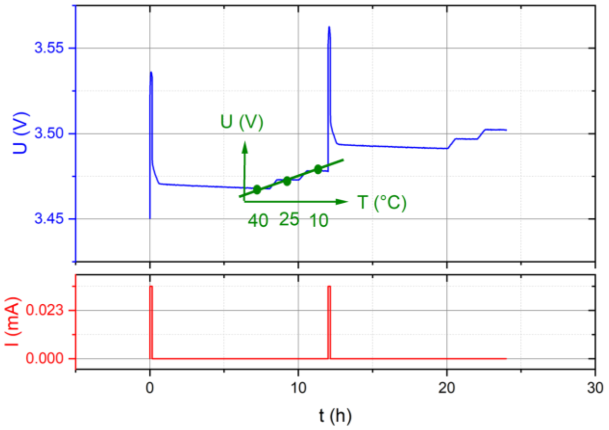

Supplementary Figure S2. *Extract of the applied GITT procedure with temperature change for entropymetry measurements. The applied current is presented in the bottom panel and the measured voltage is presented in the upper panel. The temperature was changed after each current pulse after 8h of relaxation for 2h each at 25°C and 10°C. The linear regression of the measured voltage is schematically presented in green colour.*

Discussion – The entropy measurement is performed in a coin-type battery, representing a closed system. Therefore, several cell elements potentially contribute to measured entropy change. Cell housing, electrolyte and separator are not expected to change dependent on the state of charge of the battery. Therefore, any qualitative influence of these elements on the course of the entropy change ΔS(x) can be neglected. The sodium metal counter electrode is pure bcc sodium metal, which is reported to be independent of any change in entropy during (dis)charge [2–4]. For the sodium transition metal oxide cathode, the magnetic- and nuclear entropy are not supposed to change [4]. Furthermore, Reynier et al. reported for Li_xCoO_2, that the phonon- and the electronic entropy change are negligible and approximately constant over the course of the experiment [4]. Consequently, the almost exclusive contribution to the qualitative course of the entropy change with the sodium stoichiometry is due to the configurational entropy [4]. Please note, that the quantitative course of the measured entropy change might be influence by the above discussed contributions. However, the qualitative course of the entropy change with the stoichiometry ΔS(x) is highly representative of the configurational entropy change.

Error propagation – For the entropy change results, the y-errors are included in the plots. They were calculated from the standard deviation of the linear regression parameter $\frac{\partial E}{\partial T}$, which was directly computed by Origin through least-squares fitting. Therewith, the uncertainty of the entropy change takes the form

$$\delta(\Delta S) = nF\,\delta\left(\frac{\Delta E}{\Delta T}\right) \tag{6}$$

Errors in x-direction were found to be negligible and therefore are not included in the presented figures. However, a short summary of the applied error estimation is presented in the following section. All uncertainties are listed in **Supplementary Table S1**.

The sodium stochiometries were calculated according to

$$x = x_0\left(1 - \frac{I_{dis}t_{dis} + I_{ch}t_{ch}}{m_B\,C_s}\right) \tag{7}$$

where x_0 is the as-synthesized sodium stoichiometry, I_{dis} and t_{dis} the current and time during discharge and I_{ch} and t_{ch} during charge, respectively. C_s describes the theoretical specific capacity of the active material and m_B its electrode mass loading. In general, only C_s was assumed to be precise, all other parameters might be erroneous. Not all erroneous parameters influence the overall error of the sodium stoichiometry δx in the same way. Thus, the contribution of each variable was calculated. Those estimations show, that in comparison to the error of the sodium content δx_0, all other errors can be neglected. Therefore, with the Gauß propagation of uncertainty, the error of the sodium stoichiometry amounts to

$$\delta x = \delta x_0\left|1 - \frac{I_{dis}t_{dis} + I_{ch}t_{ch}}{m_B\,C_s}\right| \tag{8}$$

The uncertainty δx_0 was obtained by standard deviation of two inductively coupled plasma optical emission spectrometry (ICP-OES) measurements. The current accuracy and the sample time were adopted from device specifications of the used potentiostat. For x, the error depends linearly on the total charge that has been exchanged. Thus, the minimal and maximal uncertainties are listed.

No additional x- and y-errors were taken into account because they are negligible when compared to the standard deviation of the linear regression parameter. Furthermore, the mean value of the voltage was used for the linear regression and therefore the y-error due to the imprecision of the potentiostat was further reduced. Additionally, since the x- and y- errors arise from temperature- and voltage accuracy, they are systematic errors introduced by the instruments and hence constant over the sodium stoichiometry. This makes weighting unnecessary. Moreover, systematic errors mostly lead to offsets of the regression line only, which does not influence the slope and therefore does not impact the calculated entropy change. The interesting aspect of those calculations regarding the uncertainty is the contribution of side reactions and phase transitions. The higher the error, the higher the probability that the entropy change is superimposed by those processes. Consequently, the standard deviation of the linear regression parameter is a suitable measure for the error introduced by the cell.

Supplementary Table S1*. Uncertainties used for error estimations for entropymetry measurements as derived from device specifications and error propagation.*

Parameter	minimal uncertainty	maximal uncertainty
E (mV)		5
I (µA)		0.1
m_B (µg)		10
t (µs)		200
x in $Na_xNi_{1/3}Mn_{2/3}O_2$	$7 \cdot 10^{-3}$	0.018
x in $Na_xMn_{3/4}Ni_{1/4}O_2$	$7 \cdot 10^{-5}$	0.015
x_0 for $Na_xNi_{1/3}Mn_{2/3}O_2$		0.015
x_0 for $Na_xMn_{3/4}Ni_{1/4}O_2$		0.009

Supplementary Information: Analysis of Diffraction data

For $Na_{2/3}Ni_{1/3}Mn_{2/3}O_2$, $Na_{0.60}Mn_{3/4}Ni_{1/4}O_2$ and $Na_{2/3}Mn_{3/4}Ni_{1/4}O_2$, the neutron diffraction (ND) and X-ray diffraction (XRD) patterns exhibit some interesting features such as super-lattice reflections and anisotropic broadening caused by stacking faults. To account for and quantify these features, the refinement procedure included (i) a joint refinement of neutron and X-ray diffraction data to obtain lattice parameters, atomic positions and site occupancies, followed by (ii) a Faults refinement to determine the probability of P3-type stacking faults [5] from XRD patterns as well as C_1C_1-type stacking faults [6] from ND patterns. In the following the refinement procedure is described in details.

Space group - As described in the manuscript, the XRD patterns of all three materials can be well indexed in $P6_3/mmc$ (SG 194), indicating a phase pure P2-type structure with additional weak reflections arising from the LLZ Na^+/vacancy ordering in the case of $Na_{2/3}Ni_{1/3}Mn_{2/3}O_2$ and $Na_{2/3}Mn_{3/4}Ni_{1/4}O_2$. The ND patterns exhibit additional reflections in the low Q region (e.g., Q = 1.47 Å^{-1}, Q = 1.57 Å^{-1}, Q = 1.86 Å^{-1}), which can be indexed as super-lattice with the super-lattice vector *k = (1/3 1/3 0)*, resulting in three symmetry groups suitable to describe the superstructure: $P6_322$ (SG182), $P\bar{3}1m$ (SG 162) and *P*312 (SG 149). Refinements using space group $P6_322$ (SG182) – offering the highest symmetry of the three options – describe the diffraction data reasonably well. Please note that $P6_3$ (SG 173), which is often reported in literature to describe the transition metal super-lattice in $Na_{2/3}Ni_{1/3}Mn_{2/3}O_2$[6,7], is a subgroup of $P6_322$ (SG182) without the two-fold axis perpendicular to the z-axis. As a result, the oxygen position is split going from 12*i* for $P6_322$ (SG182) into two 6*c* sites for $P6_3$ (SG 173), which is not necessary to describe the structure of $Na_{2/3}Ni_{1/3}Mn_{2/3}O_2$. Hence, $Na_{2/3}Ni_{1/3}Mn_{2/3}O_2$ is well described using $P6_322$ (SG182).

Occupancies of sodium sites – In general, the occupancies of sodium sites can be refined from XRD and ND patterns. However, diffraction methods are typically bulk sensitive and therefore feature the average information of the sample volume. P3-type stacking faults disturb the ABBA oxygen stacking of the P2-structure, causing local deviations in the respective sodium sites. Hence, the presence of P3-type stacking faults potentially impedes the analysis of sodium site occupancies. To support the refinement of sodium site occupancies, we have calculated the bond-valence map and bond-valence energy landscape and analysed the structure with respect to the likelihood for the presence of sodium. For the bond-valence map (BVS), the limits were set to $Na^{+1\pm0.3}$. The percolation energy between adjacent 4*f* and 6*g* sites obtained from the bond-valence energy landscape (BVEL) was found to be in the range of 0.56 eV, 0.53 eV and 0.51 eV for $Na_{2/3}Ni_{1/3}Mn_{2/3}O_2$, $Na_{2/3}Mn_{3/4}Ni_{1/4}O_2$ and $Na_{0.60}Mn_{3/4}Ni_{1/4}O_2$, respectively. The 2*a* site was found to be static (i.e., high percolation energy to any adjacent site). Based on these results, we have fixed the occupation for sodium on the 2*a* site to zero and refined the remaining sodium sites with the sum restricted to the stoichiometry as obtained from ICP-OES.

$Na_{0.60}Mn_{3/4}Ni_{1/4}O_2$ and $Na_{2/3}Mn_{3/4}Ni_{1/4}O_2$ – For $Na_{0.60}Mn_{3/4}Ni_{1/4}O_2$ and $Na_{2/3}Mn_{3/4}Ni_{1/4}O_2$, a joint refinement of ND and XRD patterns with the same weighting was performed using FullProf software [8] for each material. The Background was set as an interpolation of 19 points and 26 points, which were refined in height, for XRD and ND, respectively. Spherical harmonics were used to obtain a satisfactory fit despite the anisotropic peak broadening caused by stacking faults. The Mn and Ni occupancies were restricted to represent in sum the stoichiometry as determined with ICP-OES, however, similar results were obtained, when Mn and Ni occupancies were refined without any restrictions. Isotropic atomic displacement parameters B_{iso} were fixed based on a literature report of a similar material [9]. The obtained results are presented in **Table 2** and **Supplementary Table S7** for $Na_{0.60}Mn_{3/4}Ni_{1/4}O_2$ and $Na_{2/3}Mn_{3/4}Ni_{1/4}O_2$, respectively. These results were transferred to a Faults [10] model with the objective to refine the P3-type stacking faults [5] from the respective XRD pattern. The background, lattice parameters, atomic sites, site occupancies and displacement parameters were fixed based on the results of the preceding joint refinement. The obtained fit is presented in **Figure2**F and **Supplementary Figure S10**C for $Na_{0.60}Mn_{3/4}Ni_{1/4}O_2$ and $Na_{2/3}Mn_{3/4}Ni_{1/4}O_2$, respectively. Subsequently, a second Faults [10] model was applied to refine the stacking probability of C_1C_1-type stacking faults from the respective ND pattern. Again, background, lattice parameters, atomic sites, site occupancies, displacement parameters and additionally P3-type stacking faults were fixed. The obtained fit is presented in **Figure2**H and **Supplementary Figure S10**D for $Na_{0.60}Mn_{3/4}Ni_{1/4}O_2$ and $Na_{2/3}Mn_{3/4}Ni_{1/4}O_2$, respectively.

$Na_{2/3}Ni_{1/3}Mn_{2/3}O_2$ – The XRD pattern of $Na_{2/3}Ni_{1/3}Mn_{2/3}O_2$ exhibits a subtle split of the (110) and $(2\bar{1}0)$ reflections at Q = 2.50 $Å^{-1}$ and Q = 4.3 $Å^{-1}$, which is not accounted for when using $P6_322$ (SG182). However, an orthorhombic distortion of the initially hexagonal lattice (a ≠ b) is able to describe the observed peak splitting. Hence, the orthorhombic subgroup $C222_1$ (SG 20) was applied to fit the XRD and ND diffraction patterns of $Na_{2/3}Ni_{1/3}Mn_{2/3}O_2$. The XRD pattern exhibits less anisotropic broadening compared to the XRD patterns of $Na_{0.60}Mn_{3/4}Ni_{1/4}O_2$ and $Na_{2/3}Mn_{3/4}Ni_{1/4}O_2$, suggesting P3-type stacking faults are less frequent in $Na_{2/3}Ni_{1/3}Mn_{2/3}O_2$. However, significant broadening of the transition metal superstructure reflections are observed in the ND pattern, hinting at a significant probability for C_1C_1 stacking faults in $Na_{2/3}Ni_{1/3}Mn_{2/3}O_2$. In a first step, a joint refinement of ND and XRD patterns with the same weighting was performed using FullProf software [8]. The Background was set as an interpolation of 19 points and 26 points, which were refined in height, for XRD and ND, respectively. Spherical harmonics were used to obtain a satisfactory fit despite the anisotropic peak broadening caused by stacking faults. Isotropic atomic displacement parameters B_{iso} were fixed based on a literature report of a similar material [9]. Mn and Ni occupancies were freely refined to obtain a picture of the average Ni and Mn occupations as seen by ND. According to the joint refinement of the XRD and ND pattern 4*a* sites are occupied by 80% Mn and 20% Ni, 4*b(1)* sites are occupied by 95% Mn and 5% Ni and 4*b(2)* sites are occupied by 73% Ni and 27% Mn, resulting in a Mn/Ni ratio of approximately 2:1, which is fairly close to the transition metal ratio as obtained by ICP-OES (66:34). In a subsequent step, these results were transferred to a Faults [10] model with the objective to refine the P3-type stacking faults [5] from the XRD pattern. Due to the similar X-ray scattering of Ni and Mn, any potential discrepancy in the Ni and Mn occupations can be neglected for the analysis of the XRD pattern. In the Faults model, the background, lattice parameters, atomic sites, site occupancies and displacement parameters were fixed based on the results of the preceding joint refinement. The obtained fit is presented in **Figure2**E. To gain further insights into the transition metal ordering within the material, we have calculated Fourier maps based on the XRD and ND pattern using the maximum-entropy method (MEM) (**Supplementary Figure S3**). The XRD Fourier map clearly indicates significant electron density on 4*a*, 4*b(1)* and 4*b(2)* sites, suggesting these sites are occupied by transition metals. The ND Fourier map allows to distinguish between Ni and Mn due to the different scattering length (scattering length Ni = 10.3 fm, Mn = -3.73 fm) and locate these transition metals in the structure. 4*b(1)* and 4*b(2)* sites exhibit negative and positive nuclear densities, indicative of predominant occupation of Mn and Ni, respectively. For the 4*a* site, the nuclear density is close to zero. Since the XRD Fourier map shows electron density, this site is not empty, however the nuclear density is partly extinguished by the presence of both Ni and Mn. Since diffraction methods see the average, the absence of nuclear density on the 4*a* site might either arise from (i) a mixed occupation or (ii) C_1C_1 stacking faults or (iii) a mixture of both. To explore the effect of mixed transition metal occupations and C_1C_1 stacking faults, we have systematically varied the transition metal occupations and refined the C_1C_1 stacking fault probability, while keeping background, lattice parameters, atomic sites, displacement parameters and additionally the stacking probability of P3-type stacking faults fixed (**Supplementary Table S2** and

Supplementary Figure S4). The lowest R_p value was obtained with the structural model as presented in **Table 2**. The obtained fit is presented in **Figure2**G.

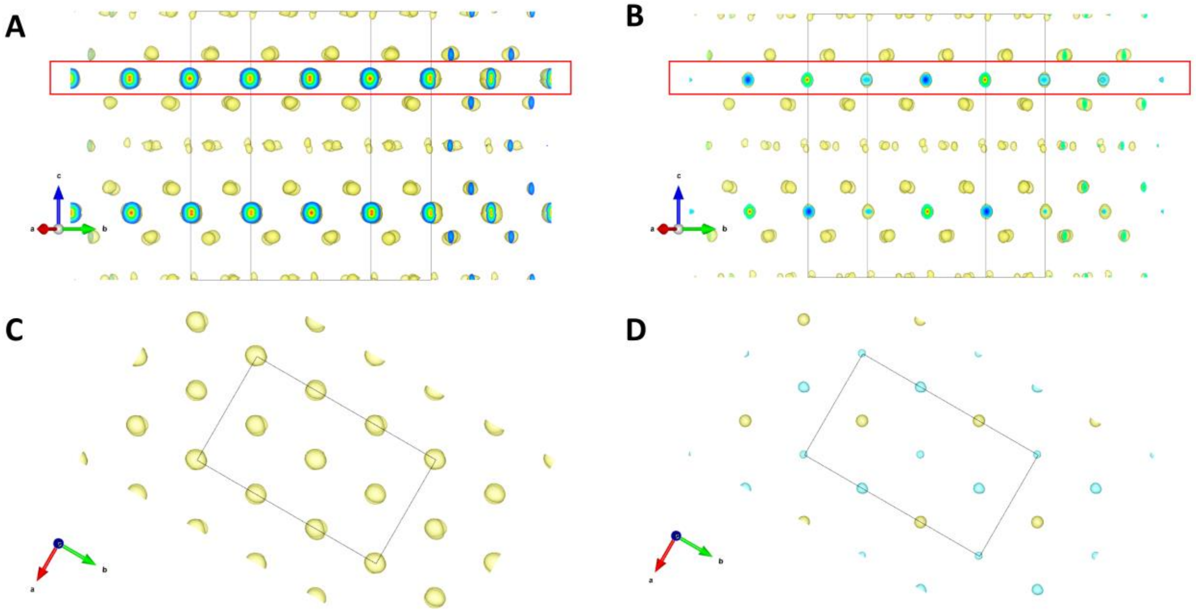

Supplementary Figure S3. *Fourier maps obtained by the maximum entropy method from the (A, C) X-ray diffraction and (B, D) neutron diffraction pattern of* $Na_{2/3}Ni_{1/3}Mn_{2/3}O_2$. *(A, B) represent the view in* $[1\,1\,\bar{2}\,0]$ *direction and (C, D) presents the view on the transition metal slab (red box in A, B, respectively) in* $[0\,0\,0\,1]$ *direction. The electron density as derived from the X-ray diffraction pattern (A, C) is similar for all transition metal sites. However, a significant difference in nuclear density between the three transition metal sites is apparent in the Fourier map derived from the neutron diffraction pattern (B, D).*

Supplementary Table S2. *Summary of FAULTS refinements applied to determine the interplay of* C_1C_1 *stacking fault probability and transition metal occupancies. Please note, that solely the* C_1C_1 *stacking probability was freely refined, while the transition metal occupancies were varied as fixed parameters. For all three transition metal sites, the Ni occupancies are balanced by Mn occupation to obtain 100 % occupation per site.*

Run #	**Ni on 4a %**	**Ni on 4b1 %**	**Ni on 4b2 %**	**P3-SFs %**	**C_1C_1-SFs %**	**R_p %**
1	0	6	100	2	4.4	5.19
2	6	0	100	2	4.4	4.96
3	8	2	96	2	4.4	4.71
4	2	8	96	2	4.8	4.98
5	10	2	94	2	4.4	4.56
6	2	10	94	2	5.7	5.00
7	6	6	94	2	4.4	4.73
8	12	0	94	2	4.4	4.56
9	14	0	92	2	4.4	4.26
10	12	4	90	2	4.4	4.46
11	10	0	96	2	4.4	4.65
12	16	0	90	2	4.4	4.37
13	18	0	88	2	4.4	4.36

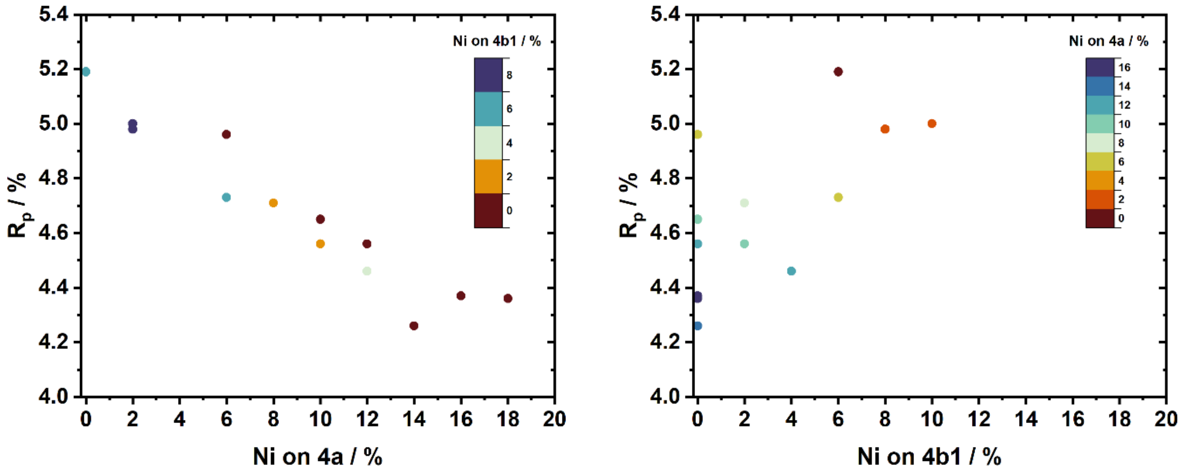

***Supplementary Figure S4**. Obtained R_p values for FAULTS refinements with various Ni occupancies on 4a and 4b(1) sites. The lowest R_p values, indicative of a suitable fitting of the diffraction data, is obtained with Ni occupations of 14 % and 0 % on 4a and 4b(1) sites, respectively. The corresponding structural model is presented in **Table 2**.*

Supplementary Experimental details

P2-$Na_{2/3}Ni_{1/3}Mn_{2/3}O_2$, P2-$Na_{3/4}Ni_{1/4}Li_{1/12}Mn_{2/3}O_2$, P2-$Na_{2/3}Ni_{1/4}Mg_{1/12}Mn_{2/3}O_2$

Synthesis - $Na_{2/3}Ni_{1/3}Mn_{2/3}O_2$, $Na_{3/4}Ni_{1/4}Li_{1/12}Mn_{2/3}O_2$, $Na_{2/3}Ni_{1/4}Mg_{1/12}Mn_{2/3}O_2$ were synthesized by mixing respective amounts of $Ni(NO_3)_2$ x 6 H_2O (Carl Roth), $Mn(NO_3)_2$ x 4 H_2O (Carl Roth), NaOH (Carl Roth), LiOH x H_2O (Carl Roth), $Mg(NO_3)_2$ x 6 H_2O (Sigma Aldrich) with fully de-ionizied water. The obtained mixture was dried at 80 °C and subsequently calcined at 900 °C for 10 h in air in a box furnace (Naberterm). The obtained powder was ground using a pulverisette 7 ball mill (Fritsch) and subsequently calcined at 900 °C for 10 h in pure oxygen in a box furnace (Carbolite Gero). After cooling to approximately 200 °C, the powder was removed from the oven and directly transferred into a Büchi glass oven, where it was kept overnight at 200 °C and dynamic vacuum (approx. 2 x 10^{-2} Pa), before being transferred inside an Argon filled glovebox (MBraun, H2O < 0.1 ppm, O2 < 0.1 ppm). Following powder handling, electrode preparation and cell assembly was performed in the same glovebox without any contact to the ambient.

Characterization results - The chemical composition was analysed using ICP-OES (Spectro Arcos SOP) in a diluted *aqua regia* solution. From the obtained quantitative analysis, a molecular formula following Na_xMO_2 (M = Ni, Mn, Li, Mg, Sc) was calculated. The obtained results are $Na_{0.649}Ni_{0.333}Mn_{0.667}O_2$, $Na_{0.729}Ni_{0.259}Li_{0.077}Mn_{0.664}O_2$ and $Na_{0.659}Ni_{0.254}Mg_{0.081}Mn_{0.664}O_2$. The crystal structure of the obtained cathode powders was analysed with X-ray powder diffraction. The obtained diffraction patterns and corresponding Rietveld Refinements using TOPAS V6 Software are presented in **Supplementary Figure S17**. All powders exhibit a P2-type structure. Solely small impurity phases such as NiO are detected. For P2-$Na_{2/3}Ni_{1/3}Mn_{2/3}O_2$ and P2-$Na_{2/3}Ni_{1/4}Mg_{1/12}Mn_{2/3}O_2$, Na^+/vacancy superstructure reflections of the LLZ-ordering are detected around Q = 2 Å^{-1}. For P2-$Na_{3/4}Ni_{1/4}Li_{1/12}Mn_{2/3}O_2$ these Na^+/vacancy superstructure reflections are absent due to the difference in sodium content. Around Q = 1.5 Å^{-1}, superstructure reflections due to the honeycomb transition metal ordering are apparent. These superstructure reflections are most pronounced, when the difference in scattering intensity is high (e.g., Li/Mn).

Electrochemistry – Slurries consisting of 90 wt.% cathode active material, 5 wt.% PVDF binder (Solvay Solef 5130) and 5 wt.% conductive carbon (Super-P-Li, Imerys) dispersed in an appropriate amount of anhydrous n-methyl-2-pyrolidone (Sigma Aldrich) were prepared inside an Argon filled glovebox. These slurries were cast on aluminium current collector foils using the doctor blade technique. Electrodes of 12 mm in diameter were punched from these films and subsequently dried in a Büchi glass oven at 130°C and dynamic vacuum overnight. Alumina coated CR2032 coin cells (Hohsen) were assembled using the dried electrodes, two layers of glass fibre separator (GFA, Whatman), 150µl 1M $NaPF_6$ in PC + 5 wt.% FEC as electrolyte and sodium metal foil serving as counter electrode. Using a galvanostatic cell test system (CTS, Basytec), cells were cycled at 57. 7 mA g^{-1}, except for check-up cycles 1, 2, 3, 25, 26, 50, 51, 75, 76, 100 and 101, which were cycled at 8.7 mA g^{-1}. Two voltage windows were used for cycling: (i) 4.3 V as upper cut-off voltage and the OCV of the as-prepared cells serving as lower cut-off voltage (denoted as "4.3 V

– OCV") and (ii) 4.3V to 1.5 V. The first voltage window ("4.3 V – OCV"), utilizes the solid solution like behaviour of these materials with the respective sodium content [7,11,12] to avoid any additional capacity due to sodiation beyond the as-synthesized sodium content.

P2-$Na_{2/3}Ni_{1/3}Mn_{2/3}O_2$, P2-$Na_{2/3}Ni_{2/9}Al_{1/9}Mn_{2/3}O_2$ and P2-$Na_{2/3}Ni_{1/3}Al_{1/9}Mn_{5/9}O_2$

Synthesis - $Na_{2/3}Ni_{1/3}Mn_{2/3}O_2$ (NM), $Na_{2/3}Ni_{2/9}Al_{1/9}Mn_{2/3}O_2$ (NAM) and $Na_{2/3}Ni_{1/3}Al_{1/9}Mn_{5/9}O_2$ (NMA) were synthesized by a co-precipitation method followed by a solid-state reaction. A stoichiometric amount of $Ni(NO_3)_2$ x 6 H_2O (Sigma Aldrich, 99.999%), $Mn(NO_3)_2$ x 4 H_2O (Sigma Aldrich, $\geq$97.0%) and $Al(NO_3)_3$ x 9 H_2O (Sigma Aldrich, 99.997%) were dissolved in water. This solution was added drop-wise to an aqueous solution of NaOH (50% excess) under an Ar atmosphere. The co-precipitated hydroxide precursors were filtered, washed until the washing water was neutral and dried overnight. The subsequent solid-state reaction was carried out, mixing the precursors with 0.685 equivalents of NaOH (Sigma Aldrich, $\geq$98%). The powder mixtures were pelletized and pre-calcined at 500 °C for 5 h and annealed at 900 °C for 6 h. The obtained CAM powders were ground and sieved (< 45 µm) and transferred into an Ar-filled glovebox (MBraun, H_2O < 0.1 ppm, O_2 < 0.1 ppm).

Characterization results – The chemical composition was analysed with ICP-OES. From the quantitative results, a molecular formula following Na_xMO_2 (M = Ni, Mn, Al) was calculated. The results are $Na_{0.65}Ni_{0.33}Mn_{0.67}O_2$, $Na_{0.64}Ni_{0.23}Al_{0.11}Mn_{0.66}O_2$ and $Na_{0.67}Ni_{0.34}Mn_{0.55}Al_{0.11}O_2$. X-ray powder diffraction (XRD) patterns of the obtained cathode materials are presented in **Supplementary Figure S18**. $Na_{2/3}Ni_{1/3}Mn_{2/3}O_2$ (NM) is a phase pure P2-type material. $Na_{2/3}Ni_{2/9}Al_{1/9}Mn_{2/3}O_2$ (NAM) and $Na_{2/3}Ni_{1/3}Al_{1/9}Mn_{5/9}O_2$ (NMA) are P2-type materials but exhibit small impurities of NiO, $Na_{0.5}Ni_{0.15}Al_{0.2}Mn_{0.65}O_2$ or $NaAlO_2$.

Electrochemistry - NAM and NMA electrodes were prepared by dispersing the NAM and NMA active material (85 wt%.), Super C65 conductive additive (10 wt%., IMERYS) and PVDF binder (5 wt%., Solvay Solef®) in NMP. The mixture was first ball milled for 2 h in a zirconia jar (milling: 1 h, rest: 10 min, repetition: 1, main disc speed: 400 rpm, rotating plates speed: 800 rpm). The obtained slurry was cast on 15 µm Al foil (Battery grade) and pre-dried at 80 °C. 12 mm diameter electrodes were punched, dried at 120 °C, pressed and dried again at 120 °C for 12 h under vacuum (mass loading: 1.7 mg cm^{-2}). Three-electrode Swagelok T-cells using NM, NAM or NMA as working electrode, Na metal (Across Organic, 99.8%) as counter and reference electrodes, 1M $NaPF_6$ (FluoroChem, battery grade) in PC as electrolyte and glass fiber (Whatman GF/D) as separator were assembled. The galvanostatic tests were performed in Maccor 4000 battery tester, applying a constant current of 17 mA g^{-1} within 1.5 - 4.3 V at 20 °C ± 2 °C.

Supplementary Figures and Tables

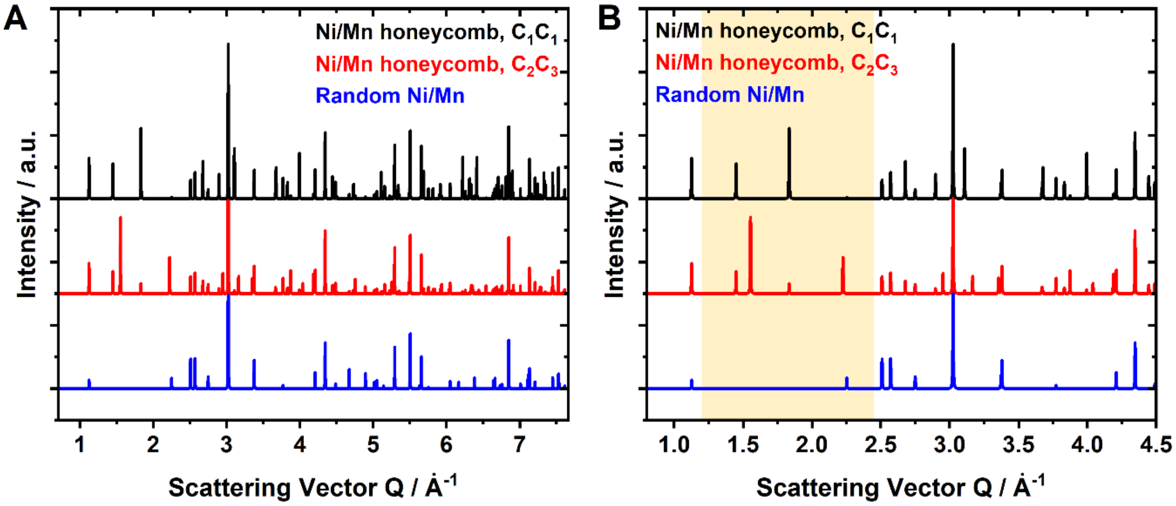

***Supplementary Figure S5**. Simulated ND patterns for the P2-$Na_{2/3}Ni_{1/3}Mn_{2/3}O_2$ assuming random Ni/Mn ordering (blue), honeycomb Ni/Mn ordering with C_2C_3 stacking sequence (red) and honeycomb Ni/Mn ordering with C_1C_1 stacking sequence (black). The presence of honeycomb Ni/Mn ordering and the nature of the stacking sequence can be clearly distinguished in the highlighted region in (B) between Q = 1.3 $Å^{-1}$ and Q = 2.4 $Å^{-1}$. Simulations have been performed using PowderCell software.*

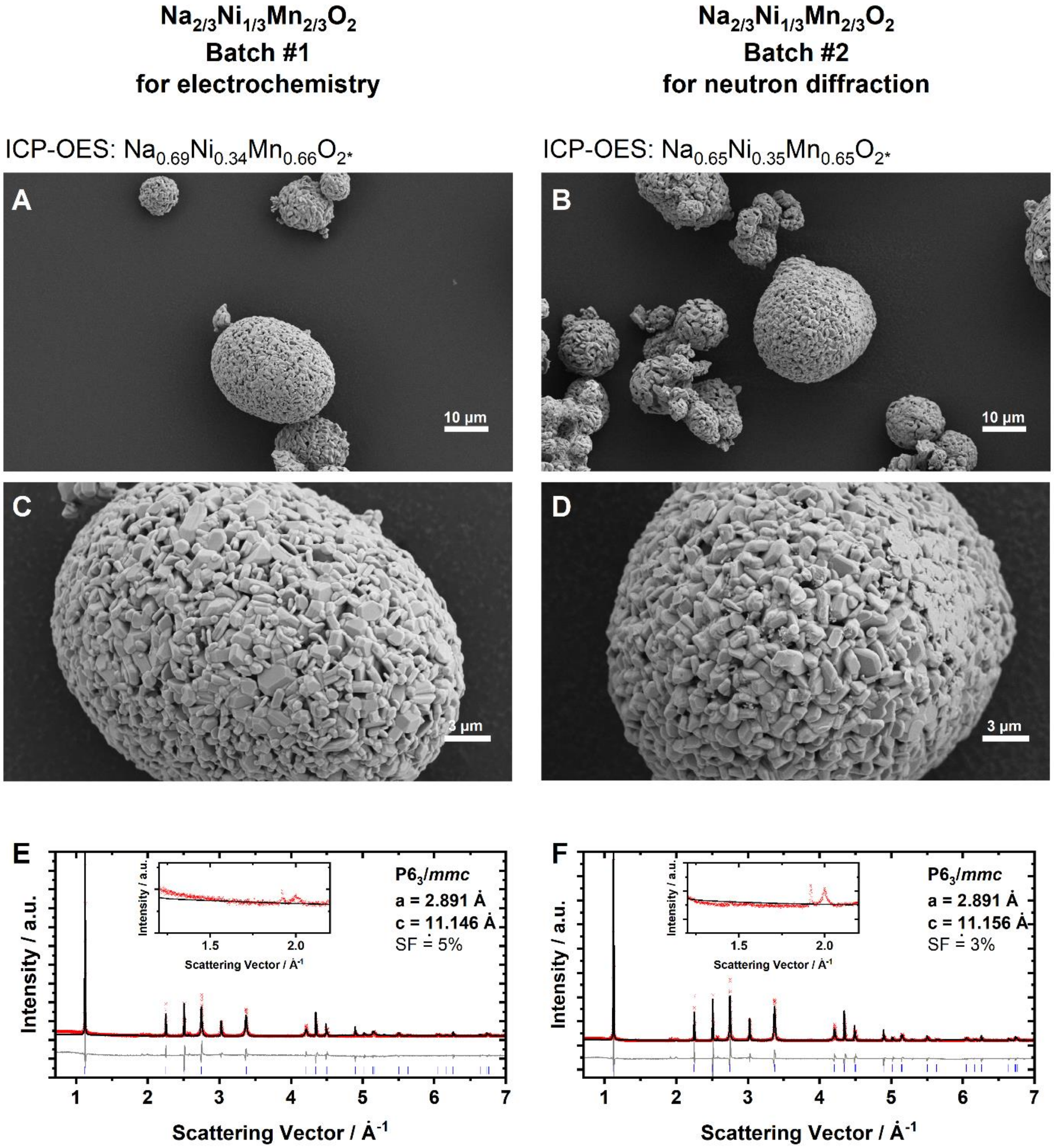

Supplementary Figure S6. *Comparison of the two batches of $Na_{2/3}Ni_{1/3}Mn_{2/3}O_2$. The chemical composition as obtained from ICP-OES analysis is presented on top. (A, C) SEM images and (E) FAULT refinement XRD pattern of the first batch used for electrochemical investigations. (B, D) SEM images and (F) FAULT refinement of XRD pattern for second batch used for neutron diffraction measurements. Detailed refinement results are presented in Supplementary Table S3 and S4. ATR-FTIR measurements of both batches are presented in Supplementary Figure S8.*

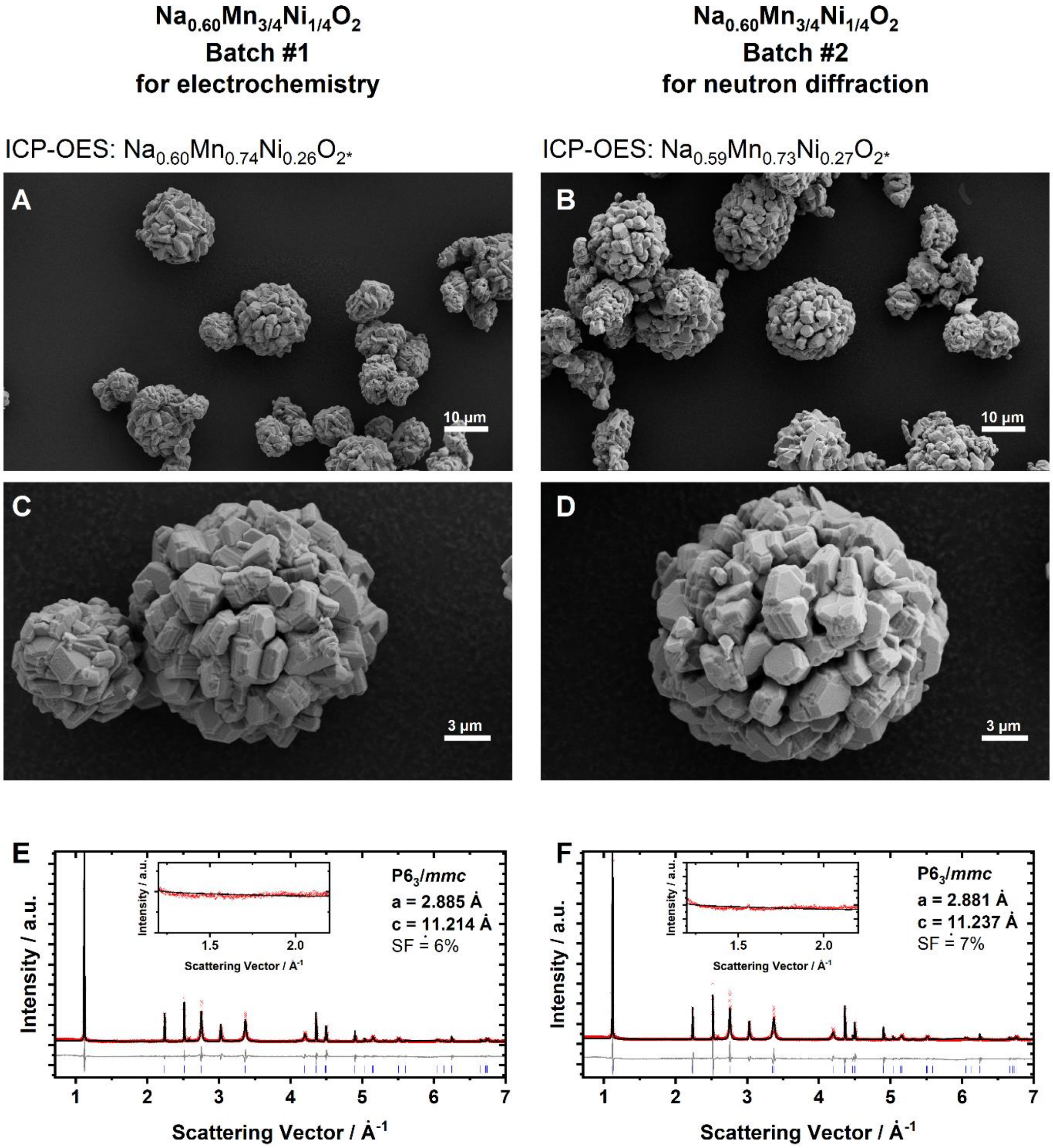

Supplementary Figure S7*. Comparison of the two batches of $Na_{0.60}Mn_{3/4}Ni_{1/4}O_2$. The chemical composition as obtained from ICP-OES analysis is presented on top. (A, C) SEM images and (E) FAULT refinement XRD pattern of the first batch used for electrochemical investigations. (B, D) SEM images and (F) FAULT refinement of XRD pattern for second batch used for neutron diffraction measurements. Detailed refinement results are presented in Supplementary Table S5 and S6. ATR-FTIR measurements of both batches are presented in Supplementary Figure S8.*

Supplementary Table S3. *Lattice parameters, P3-type stacking fault probability and Wyckoff sites for* $Na_{2/3}Ni_{1/3}Mn_{2/3}O_2$ *Batch #1 (electrochemistry) as obtained by FAULTs refinement. Values for* B_{iso} *were fixed based on Ref* [9].

SG: $P6_3/mmc$, *a* = 2.89092(1) Å, *c* = 11.1459(1) Å, V = 80.6711(1) Å³,
P3-type SFs: 4.6%, R_p = 12.81, GOF = 4.92

Atom	x	y	z	Occ	Biso
Na (2*b*)	1/3	2/3	3/4	0.39	2.526
Na (2*d*)	0	0	1/4	0.29	2.526
Mn (2*a*)	0	0	0	0.67	0.276
Ni (2*a*)	0	0	0	0.33	0.276
O (4*f*)	1/3	2/3	0.0898	1	1.105

Supplementary Table S4. *Lattice parameters, P3-type stacking fault probability and Wyckoff sites for* $Na_{2/3}Ni_{1/3}Mn_{2/3}O_2$ *Batch #2 (neutron diffraction) as obtained by FAULTs refinement. Values for* B_{iso} *were fixed based on Ref* [9].

SG: $P6_3/mmc$, *a* = 2.89120(0) Å, *c* = 11.15618(4) Å, V = 80.76113(4) Å³,
P3-type SFs: 3.0%, R_p = 7.71, GOF = 7.59

Atom	x	y	z	Occ	Biso
Na (2*b*)	1/3	2/3	3/4	0.39	2.526
Na (2*d*)	0	0	1/4	0.29	2.526
Mn (2*a*)	0	0	0	0.67	0.276
Ni (2*a*)	0	0	0	0.33	0.276
O (4*f*)	1/3	2/3	0.0898	1	1.105

Supplementary Table S5. *Lattice parameters, P3-type stacking fault probability and Wyckoff sites for* $Na_{0.60}Mn_{3/4}Ni_{1/4}O_2$ *Batch #1 (electrochemistry) as obtained by FAULTs refinement. Values for* B_{iso} *were fixed based on Ref* [9].

SG: $P6_3/mmc$, *a* = 2.88465(1) Å, *c* = 11.21362(3) Å, V = 80.80956(4) Å³,
P3-type SFs: 6.0%, R_p = 8.10, GOF = 3.82

Atom	x	y	z	Occ	Biso
Na (2*b*)	1/3	2/3	3/4	0.35	2.526
Na (2*d*)	0	0	1/4	0.25	2.526
Mn (2*a*)	0	0	0	0.75	0.276
Ni (2*a*)	0	0	0	0.25	0.276
O (4*f*)	1/3	2/3	0.0898	1	1.105

Supplementary Table S6. *Lattice parameters, P3-type stacking fault probability and Wyckoff sites for* $Na_{0.60}Mn_{3/4}Ni_{1/4}O_2$ *Batch #2 (neutron diffraction) as obtained by FAULTs refinement. Values for* B_{iso} *were fixed based on Ref* [9].

SG: $P6_3/mmc$, *a* = 2.88070(1) Å, *c* = 11.23744(4) Å, V = 80.75958(5) Å³,
P3-type SFs: 6.7%, R_p = 8.34, GOF = 7.21

Atom	x	y	z	Occ	Biso
Na (2*b*)	1/3	2/3	3/4	0.35	2.526
Na (2*d*)	0	0	1/4	0.25	2.526
Mn (2*a*)	0	0	0	0.75	0.276
Ni (2*a*)	0	0	0	0.25	0.276
O (4*f*)	1/3	2/3	0.0898	1	1.105

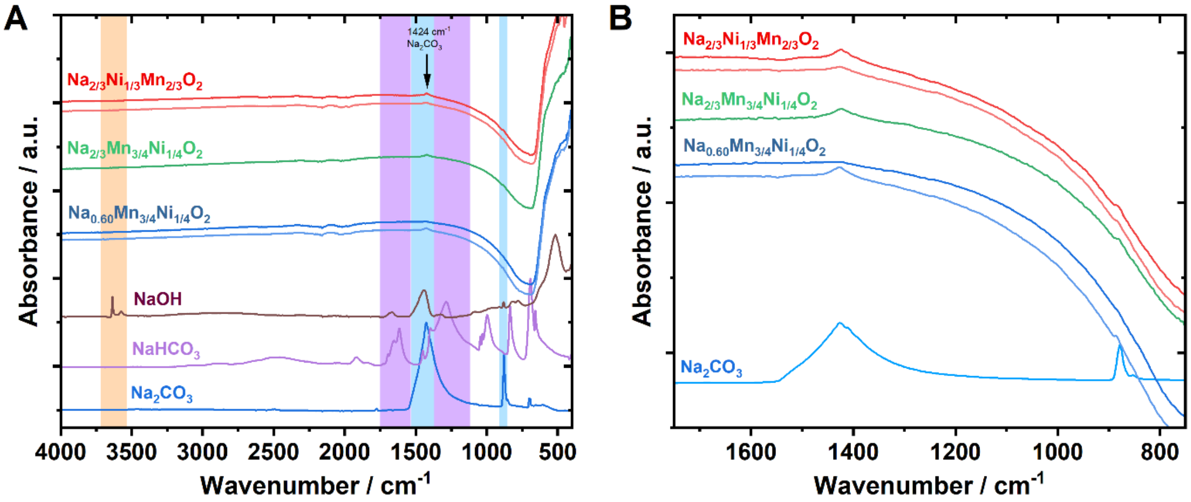

Supplementary Figure S8*. ATR-FTIR measurements for P2-$Na_{2/3}Ni_{1/3}Mn_{2/3}O_2$, P2-$Na_{2/3}Mn_{3/4}Ni_{1/4}O_2$ and P2-$Na_{0.60}Mn_{3/4}Ni_{1/4}O_2$. For P2-$Na_{2/3}Ni_{1/3}Mn_{2/3}O_2$ and P2-$Na_{0.60}Mn_{3/4}Ni_{1/4}O_2$, the upper red and blue lines represent the first batch used for electrochemistry and the lower line in light red and blue colour represents the second batch used for neutron diffraction of the respective material. Measurements for NaOH, $NaHCO_3$ and Na_2CO_3 on the same device are included for comparison.*

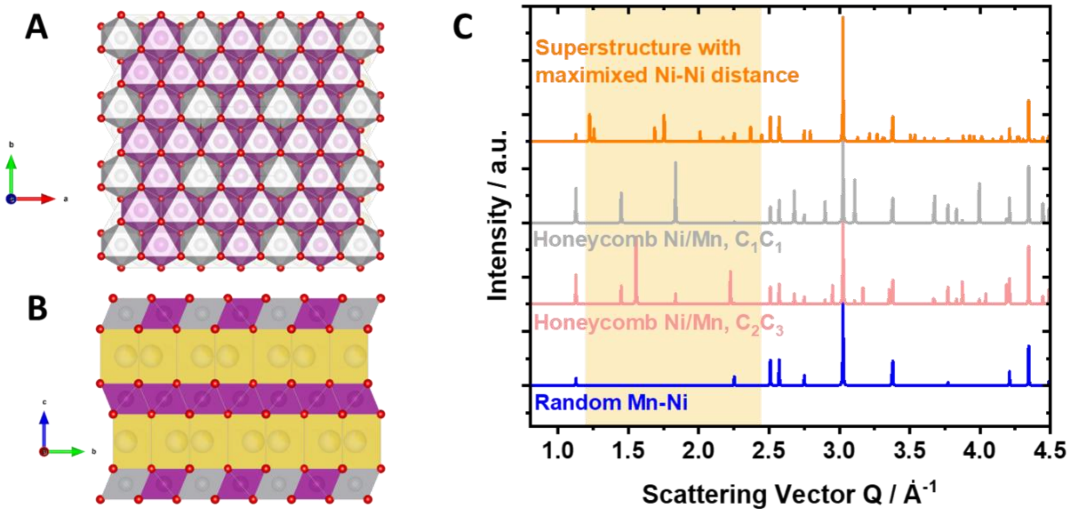

Supplementary Figure S9*. (A) View down the [001] direction on a hypothetical Ni/Mn ordering for P2-$Na_xMn_{3/4}Ni_{1/4}O_2$ under the assumption of maximized Ni-Ni distance and (B) corresponding view down the [010] direction. (C) Corresponding ND pattern as simulated using PowderCell software.*

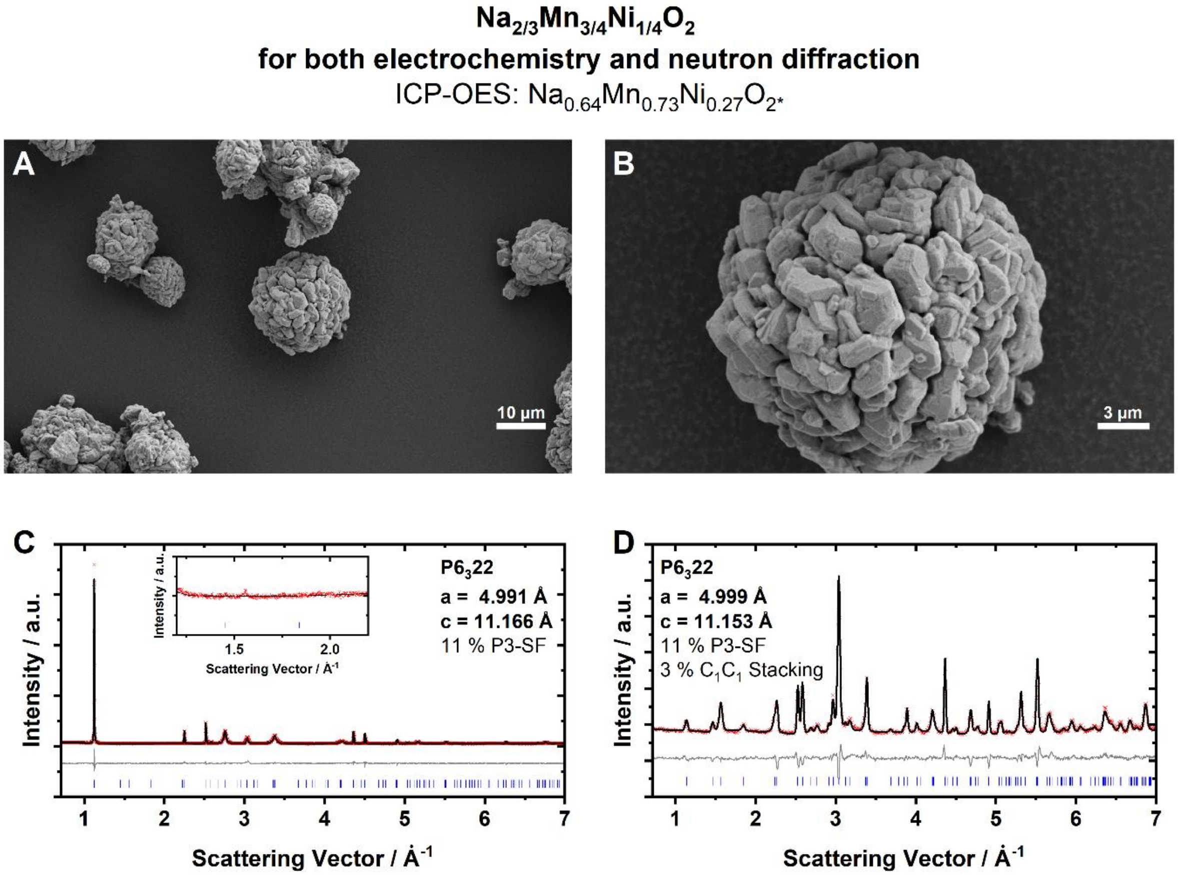

***Supplementary Figure S10**. Characterization results for P2-$Na_{2/3}Mn_{3/4}Ni_{1/4}O_2$. (A, B) SEM images of the as-synthesized powder particles, (C) refinement of X-ray diffraction pattern and (D) refinement of neutron diffraction pattern.*

***Supplementary Table S7**. Refined lattice parameters and Wyckoff sites as obtained from a joint refinement of neutron and X-ray diffraction data using FullProf Software and P3-type stacking fault probability as well as C_1C_1-type stacking fault probability as obtained from FAULTS refinement for the sample P2-$Na_{2/3}Mn_{3/4}Ni_{1/4}O_2$. Values for B_{iso} were fixed based on Ref [9].*

Refinement of ND and XRD pattern using $P6_322$ (SG 182)

ND: a = 4.9990(2) Å, c = 11.1529(9) Å, V = 241.371(25) Å³, R_p = 3.67, GOF = 2.45

XRD: a = 4.9910(1) Å, c = 11.1660(2) Å, V = 240.882(6) Å³, R_p = 4.51, GOF = 2.45

P3-type SF: 11.4 %, C_1C_1 SF: 2.8 %

Atom	x	y	z	Occ	B_{iso}
Na (4*f*)	1/3	2/3	0.0040(8)	0.2773(13)	2.526
Na (2*a*)	0	0	0	0.1870(12)	2.526
Na (6*g*)	0.3544(11)	0	0	0.4194(6)	2.526
Ni (2*c*)	1/3	2/3	1/4	0.7404(13)	0.276
Mn (2*c*)	1/3	2/3	1/4	0.2595(13)	0.276
Ni (2*d*)	1/3	2/3	3/4	0	0.276
Mn (2*d*)	1/3	2/3	3/4	1	0.276
Ni (2*b*)	0	0	1/4	0	0.276
Mn (2*b*)	0	0	1/4	1	0.276
O (12*i*)	0.3159(2)	0.3342(2)	0.8442(1)	1	1.105

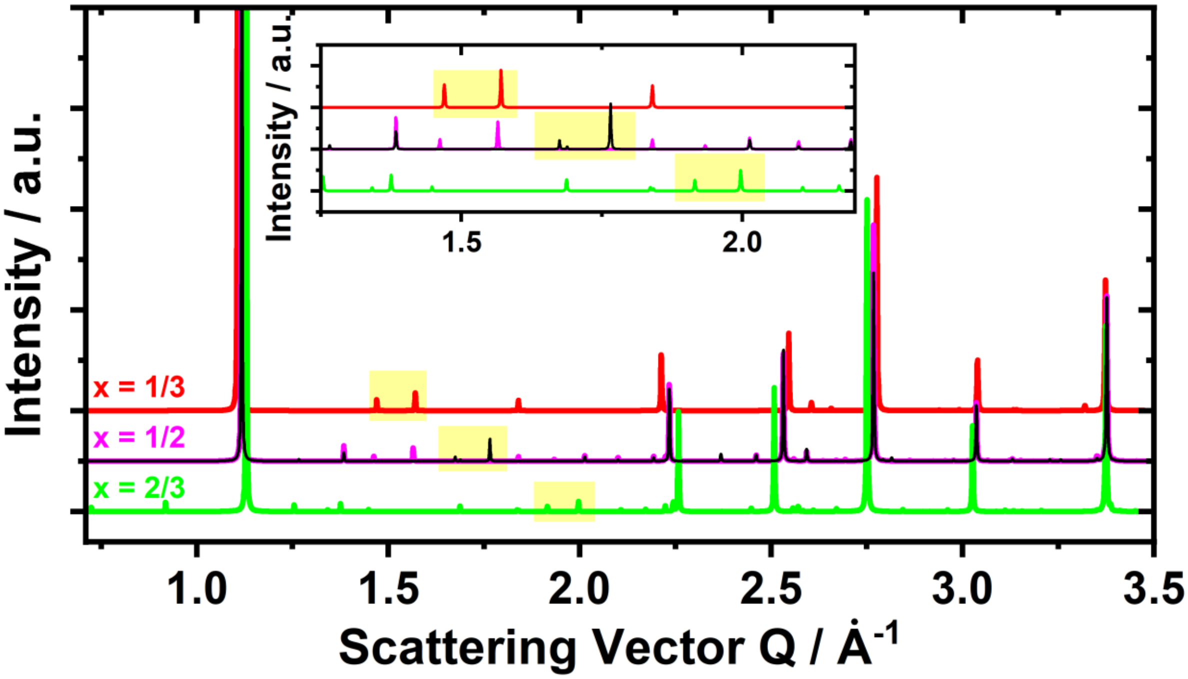

Supplementary Figure S11. *Simulated diffraction patterns of Na^+/vacancy ordered phases in P2-$Na_xNi_{1/3}Mn_{2/3}O_2$ neglecting any Ni/Mn superstructure. Diffraction patterns depicted in green, magenta and red colour are based on the Na^+/vacancy ordering as published by Lee et al.* [13]*, diffraction pattern for x = 1/2 presented in black colour is based on the Na^+/vacancy ordering as published by Huang et al.* [14]*.*

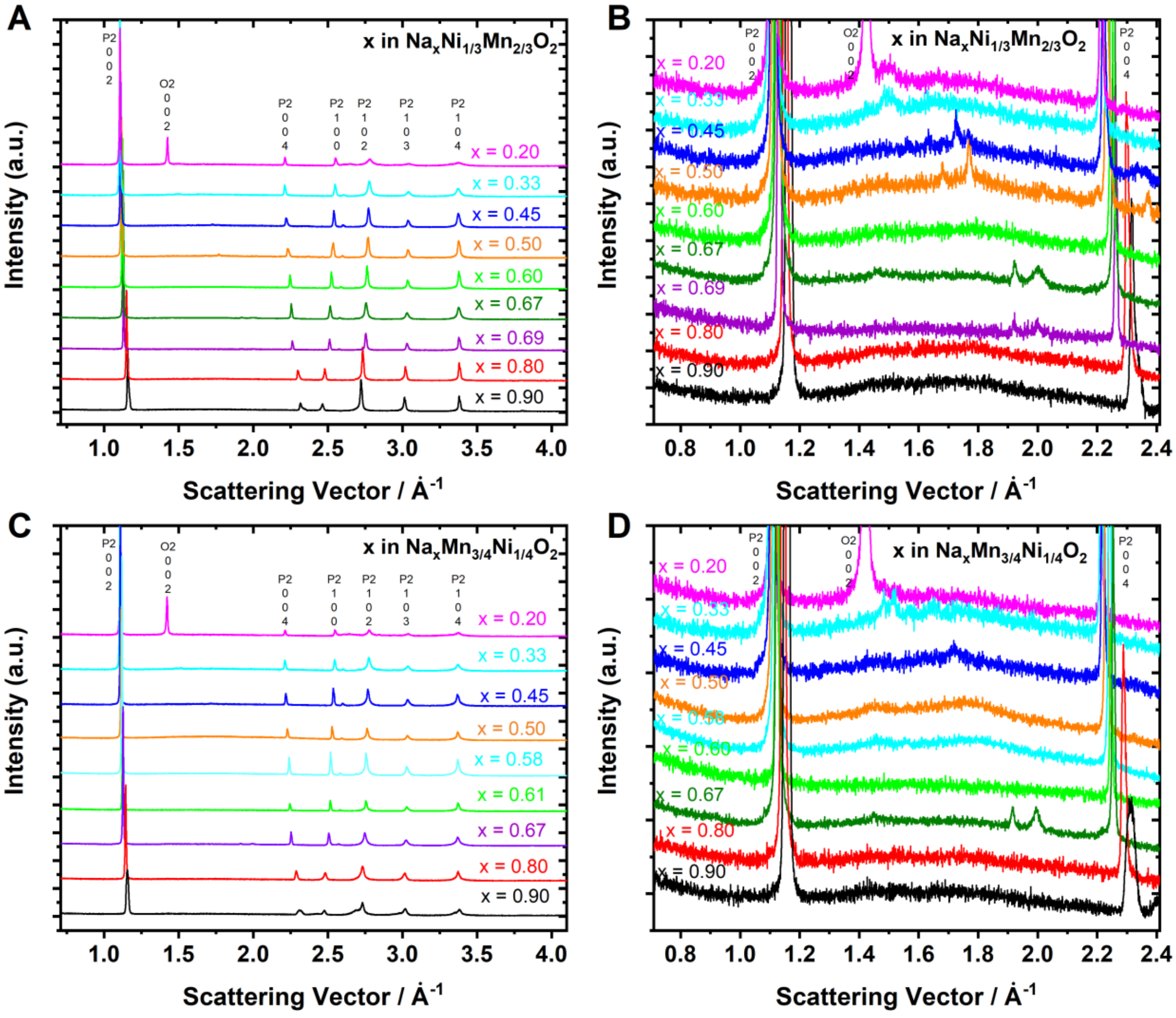

Supplementary Figure S12. *Capillary transmission X-ray diffraction patterns for (A, B) P2-$Na_xNi_{1/3}Mn_{2/3}O_2$ and (C, D) P2-$Na_xMn_{3/4}Ni_{1/4}O_2$ at various sodium contents. Superstructure reflections for respective Na+/vacancy orderings are apparent in the zoom-ins (B, D).*

Supplementary Table S8. *Estimated voltage jumps at room temperature (298 K) due to entropy change as measured with entropymetry.*

x =	**P2-$Na_xNi_{1/3}Mn_{2/3}O_2$**	**P2-$Na_xMn_{3/4}Ni_{1/4}O_2$**
2/3	0.161 V	0.046 V
0.54		0.046 V
1/2	0.188V	0.090 V
1/3	0.080 V	0.142 V

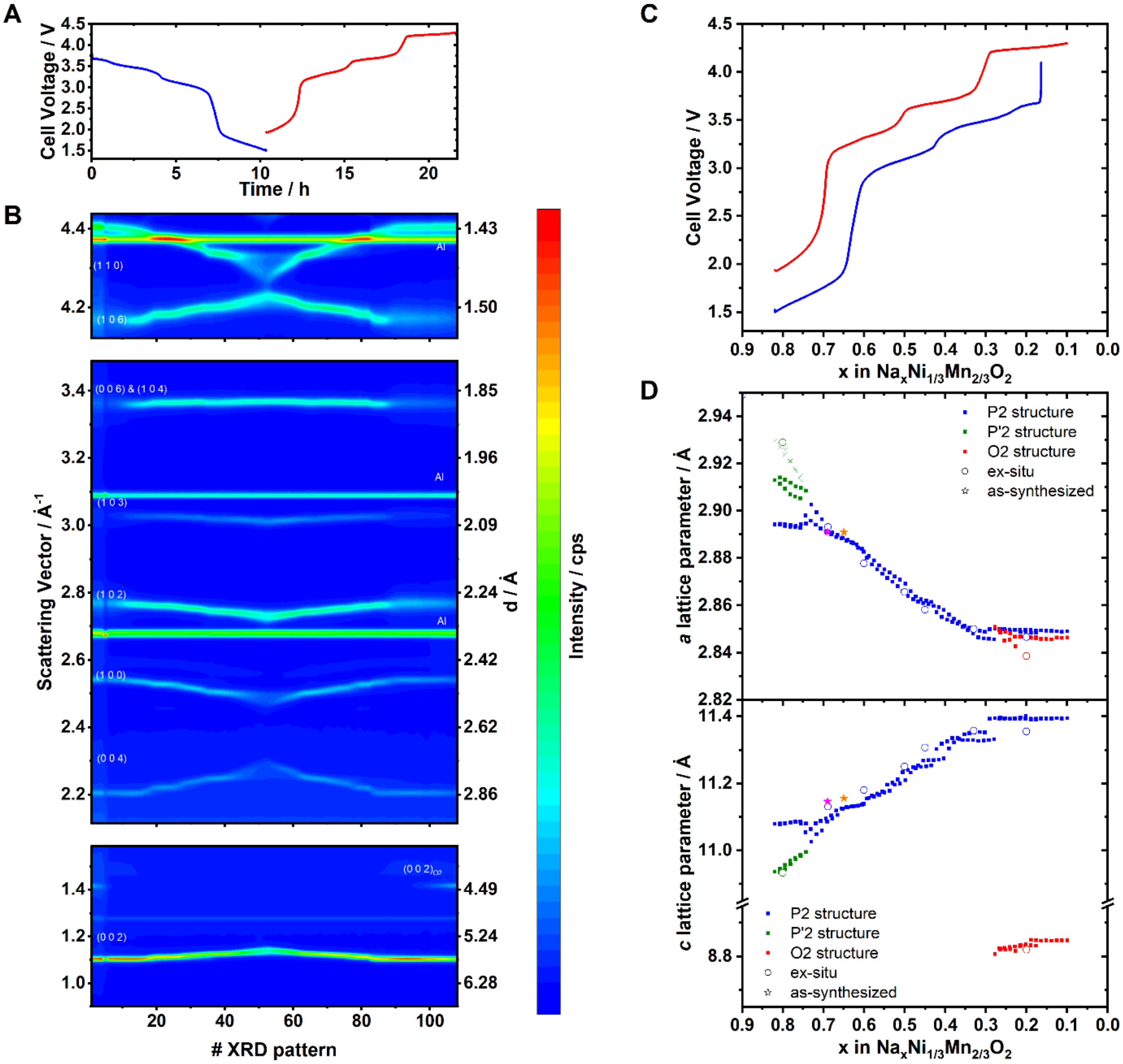

Supplementary Figure S13*. Synchrotron operando XRD data for P2-$Na_xNi_{1/3}Mn_{2/3}O_2$ and corresponding Rietveld refinement results. (A) Galvanostatic potential curve (B) heat map of collected diffraction data (C) operando voltage profile for calculated sodium contents (D) refined lattice parameters. In (D), lattice parameters obtained from operando XRD are presented as coloured squares, results from ex-situ capillary XRD as presented in Supplementary Figure S12 are depicted as circles and results from Bragg-Brentano measurements of the as-synthesized materials are presented as stars, where the magenta and orange stars correspond to the batches used for electrochemistry (Batch #1) and neutron diffraction (Batch #2), respectively. For the ease of comparison, the orthorhombic lattice parameter b_{orth} (green crosses) of the P'2 structure was transformed to the hexagonal system via $b_{hex} = \frac{b_{orth}}{\sqrt{3}}$.*

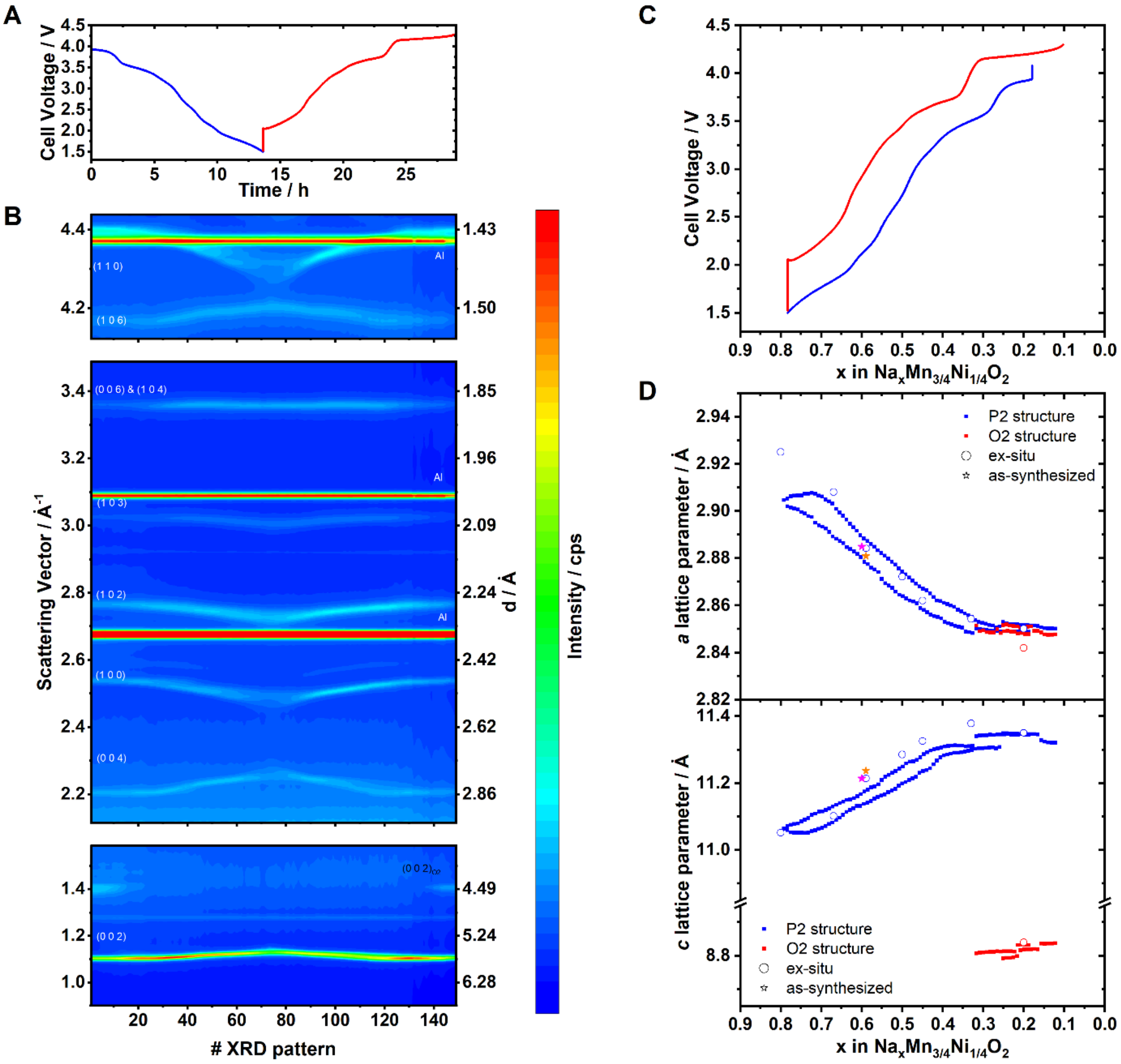

***Supplementary Figure S14**. Synchrotron operando XRD data for P2-Na$_x$Mn$_{3/4}$Ni$_{1/4}$O$_2$ and corresponding Pawley refinement results. (A) Galvanostatic potential curve (B) heat map of collected diffraction data (C) operando voltage profile for calculated sodium contents (D) refined lattice parameters. In (D), lattice parameters obtained from operando XRD are presented as coloured squares, results from ex-situ capillary XRD as presented in Supplementary Figure S12 are depicted as circles and results from Bragg-Brentano measurements of the as-synthesized materials are presented as stars, where the magenta and orange stars correspond to the batches used for electrochemistry (Batch #1) and neutron diffraction (Batch #2), respectively. The diffraction patterns obtained at high degree of sodiation exhibit strong broadening of (100) and (10l) reflections, which most likely arises from an orthorhombic distortion caused by the Jahn-Teller effect of Mn^{3+} (P'2 structure) [15]. Due to insufficient diffraction intensity, a reliable refinement of the orthorhombic P'2 structure from operando XRD pattern was not possible.*

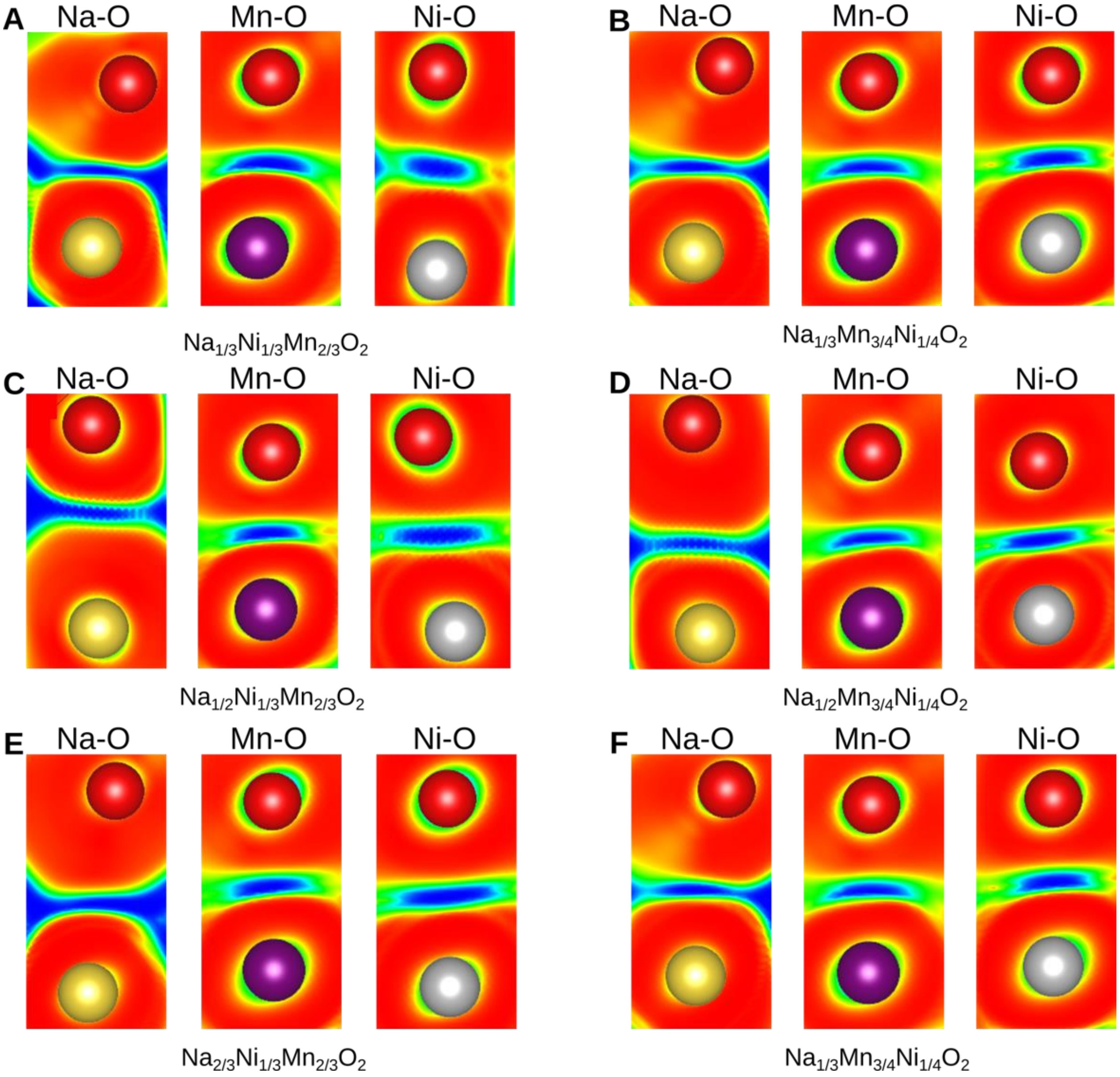

$Na_{1/3}Ni_{1/3}Mn_{2/3}O_2$

$Na_{1/3}Mn_{3/4}Ni_{1/4}O_2$

$Na_{1/2}Ni_{1/3}Mn_{2/3}O_2$

$Na_{1/2}Mn_{3/4}Ni_{1/4}O_2$

$Na_{2/3}Ni_{1/3}Mn_{2/3}O_2$

$Na_{1/3}Mn_{3/4}Ni_{1/4}O_2$

Supplementary Figure S15. *Additional DORI results for (A,C,E) P2-$Na_xNi_{1/3}Mn_{2/3}O_2$ and (B, D,F) P2-$Na_xMn_{3/4}Ni_{1/4}O_2$ at sodium contents of (A,B) x = 1/3, (C,D) x = 1/2 and (E,F) x = 2/3. DORI values of 1 imply overlapping density regions and are shown in blue while DORI values of 0 are shown in red.*

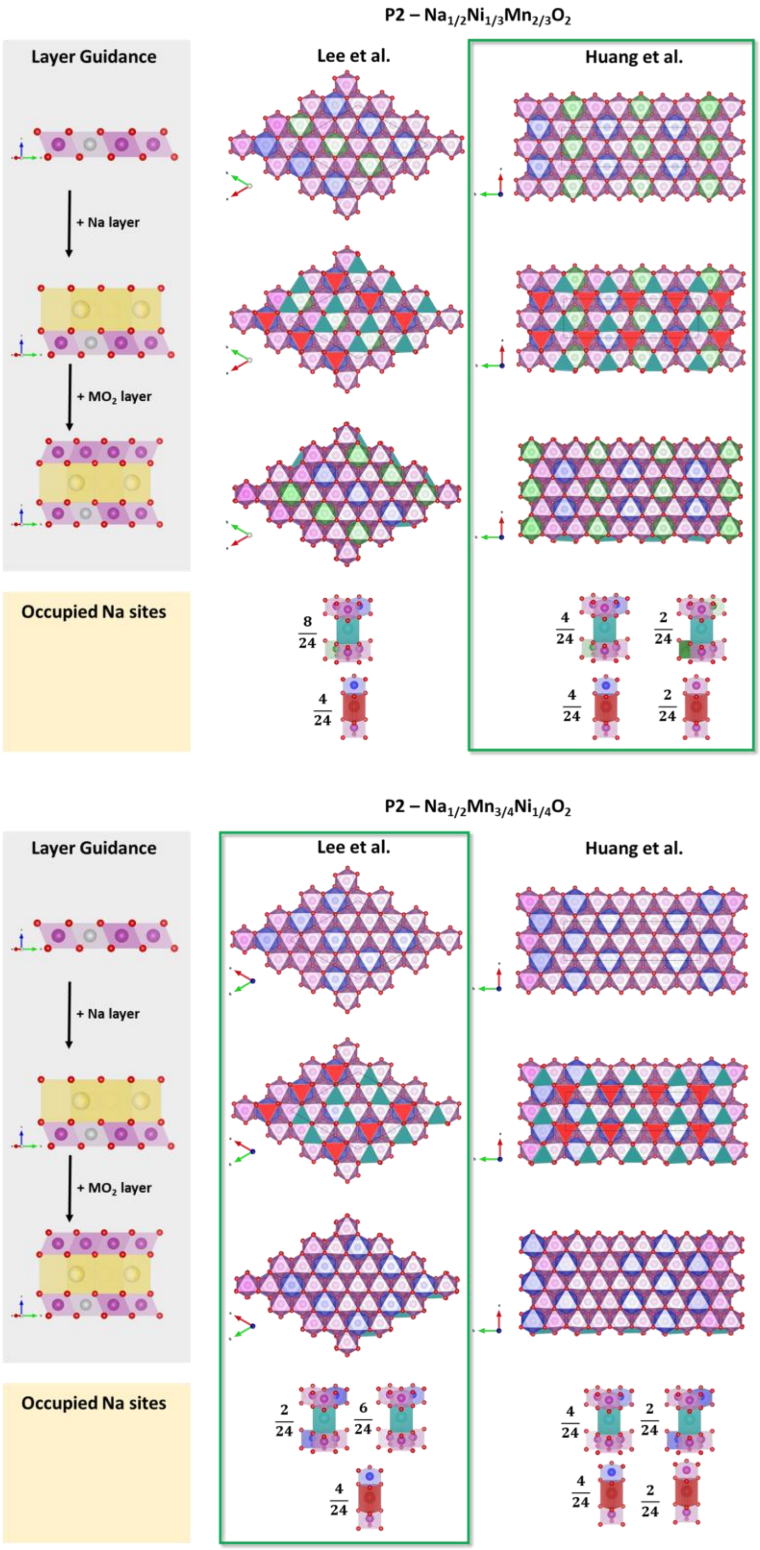

Supplementary Figure S16*. Most stable structures following the in-plane Na^+/vacancy ordering reported by Lee et al. and Huang et al. in relation to the respective transition metal charge ordering for (A) P2-$Na_xNi_{1/3}Mn_{2/3}O_2$ and (B) P2-$Na_xMn_{3/4}Ni_{1/4}O_2$. Ni^{2+}, Ni^{3+}, Mn^{3+} and Mn^{4+} are presented in blue, green, yellow and magenta colour, respectively. Na_e sites are presented in petrol colour and Na_f sites are presented in red colour.*

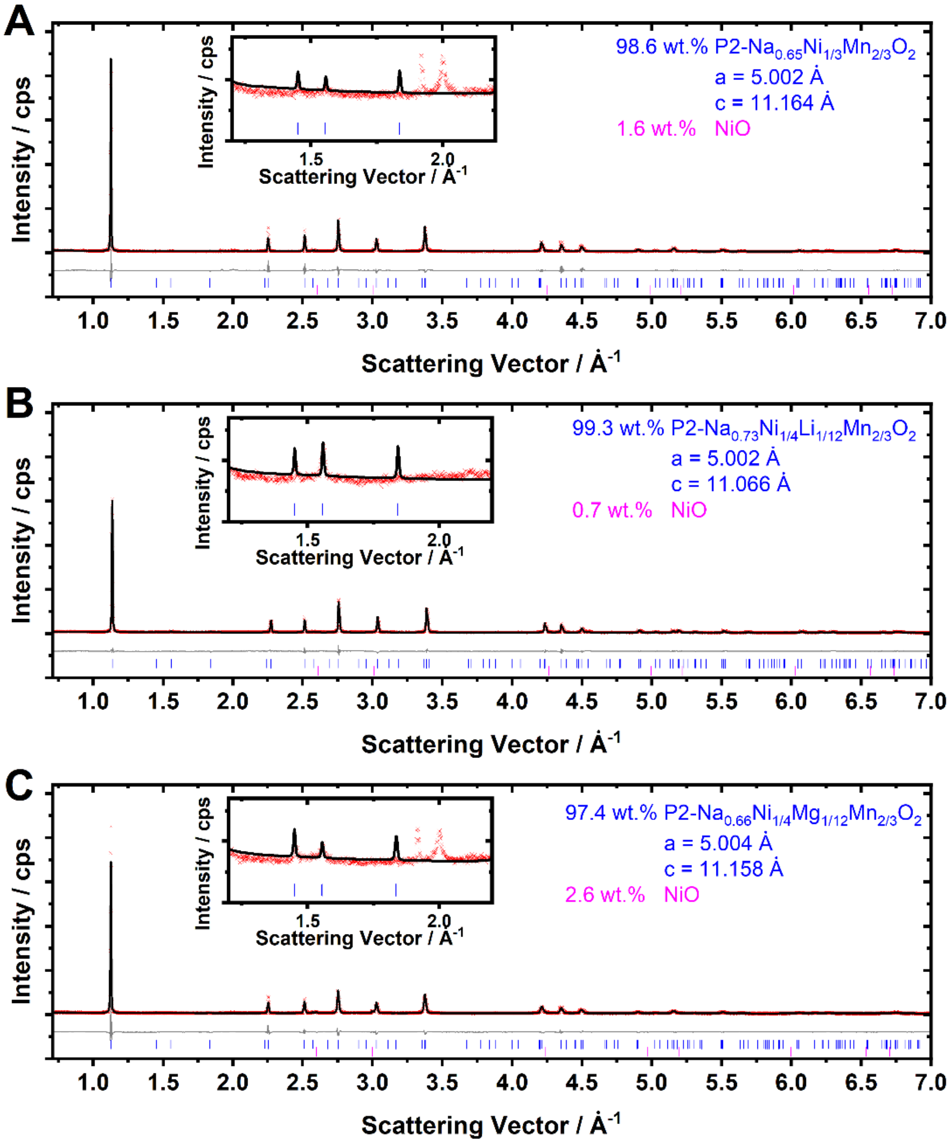

Supplementary Figure S17. *X-ray powder diffraction (XRD) patterns and corresponding Rietveld refinements of (A)* $Na_{2/3}Ni_{1/3}Mn_{2/3}O_2$, *(B)* $Na_{3/4}Ni_{1/4}Li_{1/12}Mn_{2/3}O_2$ *and (C)* $Na_{2/3}Ni_{1/4}Mg_{1/12}Mn_{2/3}O_2$. *For each diffraction pattern a zoom-in into the low-angle region is provided as insets, where the superstructure reflections of the honeycomb transition metal ordering and eventual* Na^+*/vacancy ordering superstructure reflections are apparent.*

***Supplementary Table S9**. Refined lattice parameters and Wyckoff sites as obtained from Rietveld refinement of the X-ray diffraction pattern of the P2-$Na_{2/3}Ni_{1/3}Mn_{2/3}O_2$ sample corresponding to Figure 11A and Supplementary Figure S17A. Values for B_{iso} were fixed based on Ref [9].*

Refinement of XRD pattern using $P6_322$ (SG 182)

a = 5.00245(7) Å, c = 11.1636(4) Å, V = 241.935(11) Å³,

R_p = 7.55, R_{wp} = 10.49, GOF = 3.50

Atom	**x**	**y**	**z**	**Occ**	**B_{iso}**
Na (4f)	1/3	2/3	0	0.370(5)	2.526
Na (2a)	0	0	0	0	2.526
Na (6g)	1/3	0	0	0.403(4)	2.526
Ni (2c)	1/3	2/3	1/4	1	0.276
Mn (2c)	1/3	2/3	1/4	0	0.276
Ni (2d)	1/3	2/3	3/4	0	0.276
Mn (2d)	1/3	2/3	3/4	1	0.276
Ni (2b)	0	0	1/4	0	0.276
Mn (2b)	0	0	1/4	1	0.276
O (12i)	0.3144(17)	0.3311(19)	0.8358(3)	1	1.105

***Supplementary Table S10**. Refined lattice parameters and Wyckoff sites as obtained from Rietveld refinement of the X-ray diffraction pattern of the P2-$Na_{2/3}Ni_{1/4}Mg_{1/12}Mn_{2/3}O_2$ sample corresponding to Figure 11B and Supplementary Figure S17C. Values of the isotropic displacement factor B_{iso} were fixed for Na, Ni, Mn and O based on Ref [9].*

Refinement of XRD pattern using $P6_322$ (SG 182)

a = 5.00373(9) Å, c = 11.1576(5) Å, V = 241.931(14) Å³,

R_p = 8.12, R_{wp} = 10.71, GOF = 3.21

Atom	**x**	**y**	**z**	**Occ**	**B_{iso}**
Na (4f)	1/3	2/3	0	0.383(5)	2.526
Na (2a)	0	0	0	0	2.526
Na (6g)	1/3	0	0	0.415(3)	2.526
Ni (2c)	1/3	2/3	1/4	3/4	0.276
Mg (2c)	1/3	2/3	1/4	1/4	1.000
Ni (2d)	1/3	2/3	3/4	0	0.276
Mn (2d)	1/3	2/3	3/4	1	0.276
Ni (2b)	0	0	1/4	0	0.276
Mn (2b)	0	0	1/4	1	0.276
O (12i)	0.336(2)	0.338(2)	0.8347(2)	1	1.105

***Supplementary Table S11**. Refined lattice parameters and Wyckoff sites as obtained from Rietveld refinement of the X-ray diffraction pattern of the P2-$Na_{2/3}Ni_{1/4}Li_{1/12}Mn_{2/3}O_2$ sample corresponding to Figure 11C and Supplementary Figure S17B. Values of the isotropic displacement factor B_{iso} were fixed for Na, Ni, Mn and O based on Ref [9].*

Refinement of XRD pattern using $P6_322$ (SG 182)

a = 5.00205(5) Å, c = 11.0661(3) Å, V = 239.785(8) Å^3,

R_p = 6.41, R_{wp} = 8.69, GOF = 2.67

Atom	x	y	z	Occ	B_{iso}
Na (4f)	1/3	2/3	0	0.348(8)	2.526
Na (2a)	0	0	0	0	2.526
Na (6g)	1/3	0	0	0.488(3)	2.526
Ni (2c)	1/3	2/3	1/4	3/4	0.276
Li (2c)	1/3	2/3	1/4	1/4	1.000
Ni (2d)	1/3	2/3	3/4	0	0.276
Mn (2d)	1/3	2/3	3/4	1	0.276
Ni (2b)	0	0	1/4	0	0.276
Mn (2b)	0	0	1/4	1	0.276
O (12i)	0.3426(10)	0.3424(10)	0.83663(18)	1	1.105

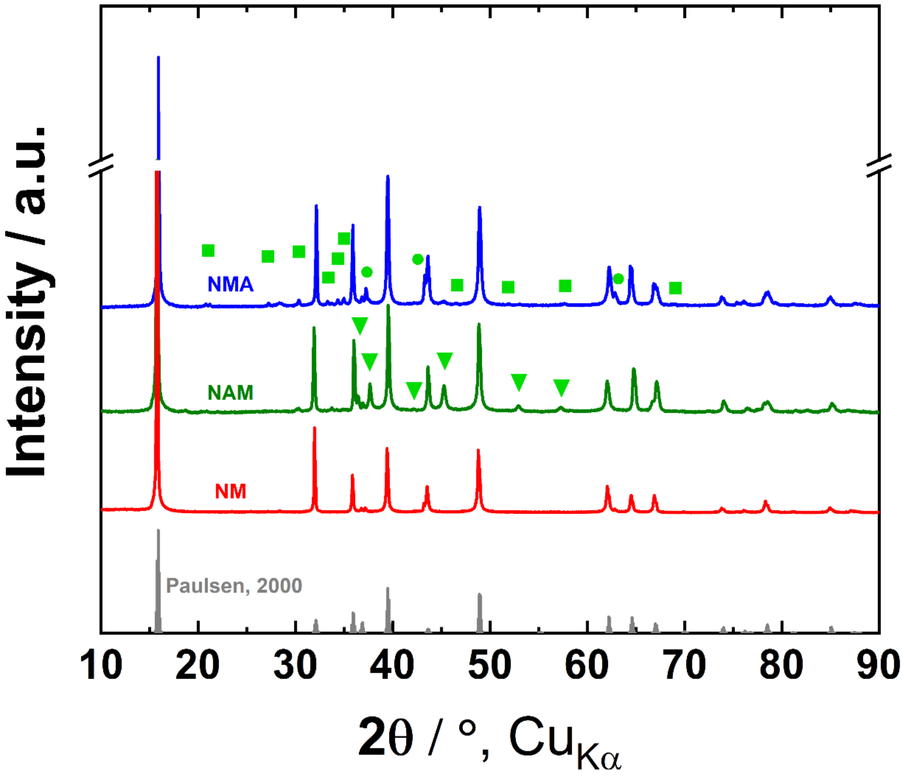

***Supplementary Figure S18**. X-ray powder diffraction (XRD) pattern of $Na_{2/3}Ni_{1/3}Mn_{2/3}O_2$ (NM), $Na_{2/3}Ni_{2/9}Al_{1/9}Mn_{2/3}O_2$ (NAM) and $Na_{2/3}Ni_{1/3}Al_{1/9}Mn_{5/9}O_2$ (NMA). Diffraction pattern presented in grey colour (Paulsen, 2000) corresponds to reference [6]. Green triangles (▼) correspond to $Na_{0.5}Ni_{0.15}Al_{0.2}Mn_{0.65}O_2$ in PDF 00-054-0839, green boxes (■) correspond to $NaAlO_2$ in reference [16] and green circles (•) correspond to NiO in reference [17].*

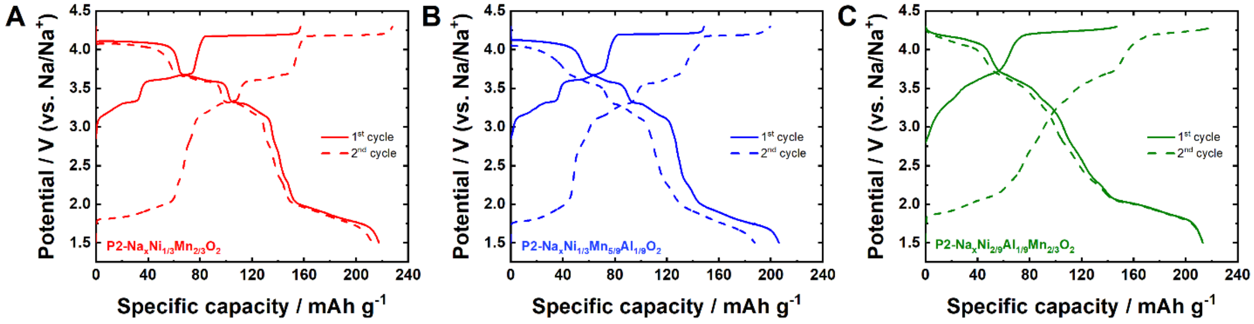

Supplementary Figure S19. *First and second cycle potential profiles in the potential range 4.3 V – 1.5 V of (A) P2-*$Na_xNi_{1/3}Mn_{2/3}O_2$ *(NM), (B)* $Na_xNi_{1/3}Mn_{5/9}Al_{1/9}O_2$ *(NMA) and (C) P2-*$Na_xNi_{2/9}Al_{1/9}Mn_{2/3}O_2$ *(NAM). Potential jumps around 3.0 V, 3.5 V and 4.0 V correspond to* Na^+*/vacancy ordering at x = 2/3, 1/2 and 1/3, respectively.*

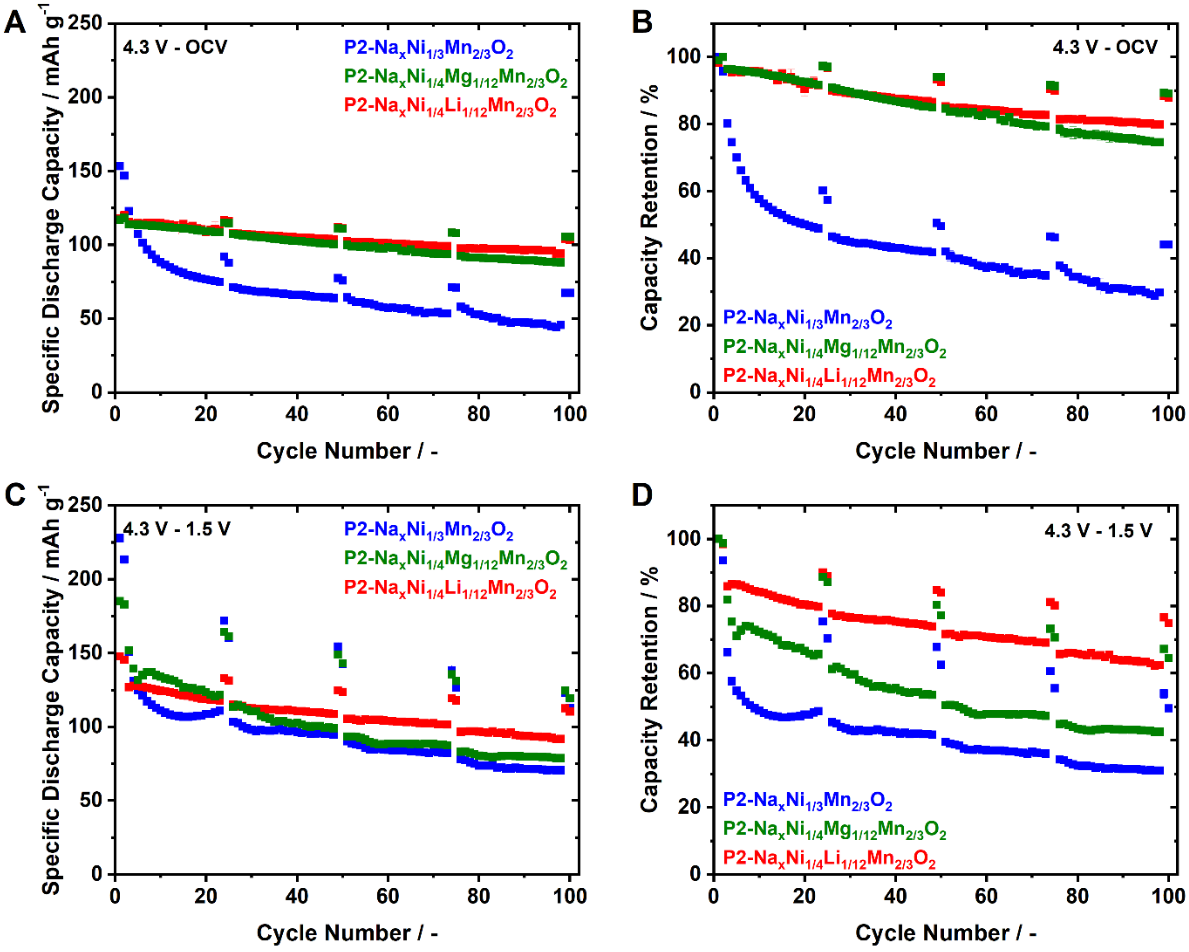

Supplementary Figure S20. *Cycling stability of P2-*$Na_{2/3}Ni_{1/3}Mn_{2/3}O_2$ *(blue), P2-*$Na_{2/3}Ni_{1/4}Mg_{1/12}Mn_{2/3}O_2$ *(green) and P2-*$Na_{3/4}Ni_{1/4}Li_{1/12}Mn_{2/3}O_2$ *(red) in sodium half-cells. Cells were cycled at 57. 7 mA g*$^{-1}$*, except for check-up cycles 1, 2, 3, 25, 26, 50, 51, 75, 76, 100 and 101 which were cycled at 8.7 mA g*$^{-1}$*. For (A) and (B), cells were cycled with an upper cut-off voltage of 4.3 V and the OCV of the as-prepared cells serving as lower cut-off voltage. For (C) and (D) cells were cycled between 4.3 V and 1.5 V. (A) and (C) present the course of the specific capacity over 101 cycles. (B) and (D) present the course of the capacity retention. For both voltage windows and each material, the presented data depicts the average obtained from at least two cells and the standard deviation is depicted as error bars.*

References

1 A. J. Bard and L. R. Faulkner, *Electrochemical methods. Fundamentals and applications*, Wiley, New York, Weinheim, 2nd edn., 2001.

2 V. V. Viswanathan, D. Choi, D. Wang, W. Xu, S. Towne, R. E. Williford, J.-G. Zhang, J. Liu and Z. Yang, *Journal of Power Sources*, 2010, **195**, 3720–3729.

3 K. Jalkanen and K. Vuorilehto, *Journal of Power Sources*, 2015, **273**, 351–359.

4 Y. Reynier, J. Graetz, T. Swan-Wood, P. Rez, R. Yazami and B. Fultz, *Phys. Rev. B*, 2004, **70**, 753.

5 L. F. Pfeiffer, N. Jobst, C. Gauckler, M. Lindén, M. Marinaro, S. Passerini, M. Wohlfahrt-Mehrens and P. Axmann, *Front. Energy Res.*, 2022, **10**, 305.

6 J. M. Paulsen, R. A. Donaberger and J. R. Dahn, *Chem. Mater.*, 2000, **12**, 2257–2267.

7 N. Tapia-Ruiz, W. M. Dose, N. Sharma, H. Chen, J. Heath, J. W. Somerville, U. Maitra, M. S. Islam and P. G. Bruce, *Energy Environ. Sci.*, 2018, **11**, 1470–1479.

8 J. Rodríguez-Carvajal, *Physica B: Condensed Matter*, 1993, **192**, 55–69.

9 J. W. Somerville, A. Sobkowiak, N. Tapia-Ruiz, J. Billaud, J. G. Lozano, R. A. House, L. C. Gallington, T. Ericsson, L. Häggström, M. R. Roberts, U. Maitra and P. G. Bruce, *Energy Environ. Sci.*, 2019, **12**, 2223–2232.

10 M. Casas-Cabanas, M. Reynaud, J. Rikarte, P. Horbach and J. Rodríguez-Carvajal, *J Appl Crystallogr*, 2016, **49**, 2259–2269.

11 Z. Lu and J. R. Dahn, *Chem. Mater.*, 2001, **148**, A1225.

12 J. Xu, D. H. Lee, R. J. Clément, X. Yu, M. Leskes, A. J. Pell, G. Pintacuda, X.-Q. Yang, C. P. Grey and Y. S. Meng, *Chem. Mater.*, 2014, **26**, 1260–1269.

13 D. H. Lee, J. Xu and Y. S. Meng, *Physical chemistry chemical physics : PCCP*, 2013, **15**, 3304–3312.

14 Q. Huang, M. L. Foo, J. W. Lynn, H. W. Zandbergen, G. Lawes, Y. Wang, B. H. Toby, A. P. Ramirez, N. P. Ong and R. J. Cava, *Journal of Solid State Chemistry*, 2004, **16**, 5803–5814.

15 L. F. Pfeiffer, Y. Li, M. Mundszinger, J. Geisler, C. Pfeifer, D. Mikhailova, A. Omar, V. Baran, J. Biskupek, U. Kaiser, P. Adelhelm, M. Wohlfahrt-Mehrens, S. Passerini and P. Axmann, *Chem. Mater.*, 2023, **35**, 8065–8080.

16 N. V. Proskurnina, V. I. Voronin, G. S. Shekhtman and N. A. Kabanova, *Ionics*, 2020, **26**, 2917–2926.

17 S. SASAKI, K. FUJINO and Y. TAKÉUCHI, *Proc. Jpn. Acad., Ser. B*, 1979, **55**, 43–48.